



UNIVERSITEIT VAN AMSTERDAM



VRIJE
UNIVERSITEIT
AMSTERDAM

Research Thesis Master's Chemistry

Reduced ion migration in 2D/3D perovskite solar cells

By

Rens van Roosmalen

June 30th 2021

Student number

11048549

Research institute

AMOLF

Research group

Hybrid Solar Cells

Supervisor

prof. dr. B. Ehrler

Examiners

prof. dr. E.C. Garnett, dr. R.M. Williams

Table of Contents

Table of Contents	3
Abstract	4
Introduction	5
Perovskite solar cells	5
Stability and ion migration	6
2D perovskite solar cells	7
2D/3D perovskite solar cells	8
Supramolecular design principles in 2D/3D perovskites	9
Ion migration measurements	10
Methods	11
Device fabrication	11
Electrical measurements	11
TID – Data analysis	12
Results and discussion	13
Thermal admittance spectroscopy – TAS	13
Capacitance Voltage measurements – CV	14
Transient Ion-Drift – TID	15
Comparative analysis	19
Assignment of processes to physical migration pathways	25
Conclusion and Outlook	26
Appendix	28
References	32
Acknowledgements	36

Abstract

In this work, the ion migration in different perovskite solar cells is examined using Transient Ion-Drift, since ion migration is frequently related to long-term stability issues. A 3D hybrid organic-inorganic perovskite solar cell is used as a reference device to compare with 2D/3D perovskite systems. These 2D/3D systems consist of bulk 3D perovskite, with a small 2D perovskite layer between the hole transport layer and the bulk 3D perovskite. The 2D perovskite layers are known to enhance the long-term stability of perovskite solar cells, a key issue for large-scale perovskite solar cell application. However, there is only limited knowledge on how the ion migration is influenced by this layer. To study this, we use three different 2D/3D systems, based on different supramolecular interactions of the organic spacers: PhenEthylAmmonium (PEA), pentaFluorophenEthylAmmonium (FEA) and mixed PEA/FEA spacers. To quantify the ion migration in these 2D/3D systems and the reference 3D system, we use TID spectroscopy, which is a capacitance-based technique used in semiconductor devices.

We find that the same three processes occur in all four examined systems. The first process is attributed to the migration of iodide and this process is decreased in the 2D/3D systems containing PEA spacers. This decrease in ion migration is expressed in a higher activation energy for migration and in a reduced concentration of mobile ions. The second process is constant across all devices and requires more investigation towards assignment as migration of ions or as a trapping effect. The last process is likely due to an interface effect at TiO_2 and is also found to be relatively constant throughout all of the measured devices. Since two out of three processes remain constant, the increased stability in 2D/3D systems appears to be caused by the reduction of iodide migration, likely in combination with another mechanism not related to ion migration. This work thus allows us to assign and quantify the reduced iodide migration in PEA-based 2D/3D systems, opening a pathway to further mechanistic studies.

Introduction

Climate change is one of the most serious issues in our society, anthropogenic emission of greenhouse gases causes the globe to warm up faster than in natural climate cycles.^{1,2} The majority of these emissions are related to fossil fuel combustion for energy.³ This energy could instead be harnessed from sustainable sources, such as the sun, which annually provides enough energy to cover the global energy consumption 40.000 times.⁴ However, the share of photovoltaic electricity remains limited, with only ~1% of the global energy market generated by photovoltaics in 2019.⁵ While silicon-based PhotoVoltaics (PV) have shown gradual growth in technological aspects and economic feasibility, more flexible technology with higher efficiencies can be uncovered by exploring alternative technologies.^{6,7}

Perovskite solar cells

Perovskite solar cells have gained significant attention over the past years, as they are excellent and tuneable absorber materials, quickly resulting in cells with Power Conversion Efficiencies (PCE) of up to 25.2%.^{8,9} Since perovskite solar cells can be made in a low-temperature, solution-based process, there is significant potential for low-cost fabrication, further enhancing economic feasibility. Such perovskite materials have an ABX_3 structure (Figure 1), where B is a divalent cation, surrounded by 6 anions (X_3) to form a corner-sharing octahedral structure.

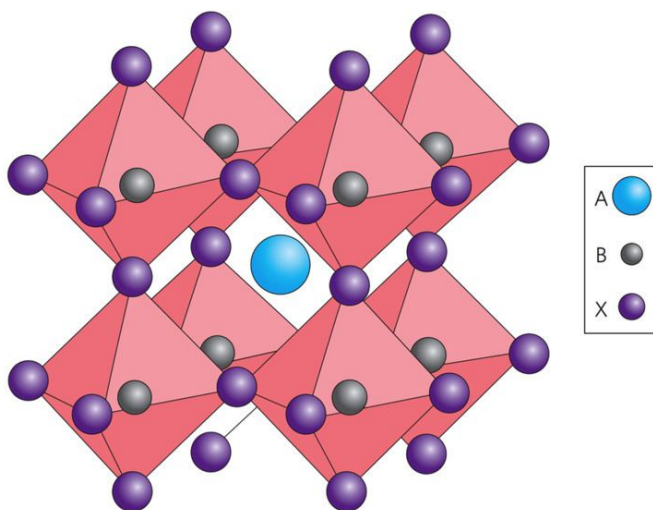


Figure 1 - Perovskite ABX_3 structure, A and B are cations, X is an anion. Reproduced from Alchetron.¹⁰

The A-site is another cation, which is positioned in the cavities between the octahedra. There is a significant range of ions that can be used to form a perovskite, allowing for tunability of opto-electronic properties, such as the bandgap.¹¹ Since perovskites have a large defect tolerance, forming the structure is relatively straightforward.^{12,13} The bonds in perovskites are partially ionic and partially covalent, resulting in a relatively unique feature: the perovskite semiconductors have both electronic and ionic conductivity.¹⁴ Methylammonium lead triiodide ($MAPbI_3$) is a well-studied perovskite material with a sharp absorption edge, high absorption coefficient, long carrier lifetimes and a large carrier diffusion length. $MAPbI_3$ is

therefore commonly used as a prototypical perovskite material.¹⁵ MAPbI₃ is easily altered by changing the composition; many dopants can be added, different halides can be used, both pure halide (Cl, Br, I) and mixed-halide perovskites are viable.¹⁶ Due to the tunability of the bandgap, perovskites can be tailored to match the absorption spectra of other types of solar cells, making them a promising candidate for tandem applications. However, the stability of perovskite solar cells remains a major challenge.¹⁷

Stability and ion migration

For real-world application, solar cells need to be stable for 20-25 years, which is not yet the case for perovskite solar cells. The soft ionic nature of perovskites causes extreme sensitivity to external factors, such as moisture and oxygen, which can be alleviated by proper encapsulation.¹⁸ However, the soft crystal structure itself also results in complex internal events that can be related to instability. Indeed, the soft crystal structure induces crystal defects and their concentration depends on fabrication and utilisation of the perovskite.¹⁹ These imperfections in the crystal lattice result in the formation of electronic trap states and allow movement of ions, resulting in complex dynamic properties of perovskite solar cells under light-operation or electronic bias. This movement of ions in the perovskite ABX₃ structure is called ion migration and is related to long-term degradation and reduced efficiency during operation. This phenomenon can be mediated by vacancies, interstitials or antisite substitutions (Figure 2).

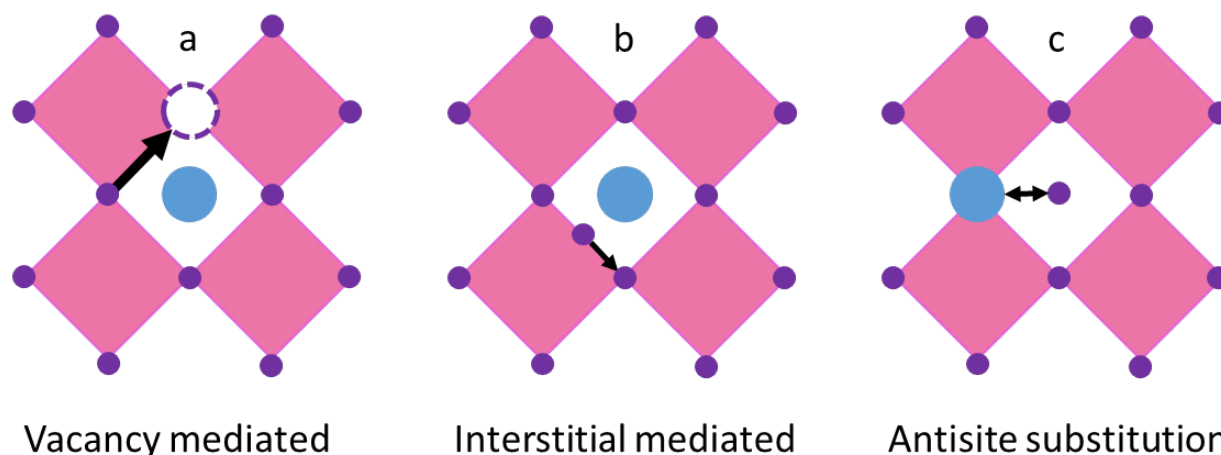


Figure 2 – Ion migration pathways in perovskite solar cells. a) vacancy-mediated, b) interstitial-mediated and c) antisite substitution

While both the anions and the cations can migrate in MAPbI₃, the activation energies (E_A) differ for each ion, with a wide range of reported values: 0.08–0.58 eV for iodide, 0.46–1.12 eV for methylammonium and 0.80–2.31 eV for lead.^{20–24} However, both experimental and simulated experiments result in the same trend in activation energies: I⁻ has the lowest barrier, followed by MA⁺, and Pb²⁺ has the highest E_A for ion migration. Since the activation energy of Pb²⁺ is relatively high, most practical cases only consider the migration of I⁻ and MA⁺.

During device operation, ions migrate towards the charge-extraction interface, causing accumulation, which induces a change in the internal electric field and in the effective work functions of the transport layers.²⁵ Both of these effects can cause a reduced efficiency in the solar cell, by reducing the charge extraction rates. Besides accumulation at the interface, penetration in the transport layers has been

observed. Indeed, both MA^+ and I^- can enter these layers, causing chemical reactions that prevent charge extraction and causing disorder of the structure in the layer, severely reducing conductivity, and thus the PCE.^{26,27}

Ion migration also causes stability issues in the bulk of the perovskite, a typical example occurs in mixed-halide perovskites, as these suffer from phase segregation during illumination.^{28,29} The initially well-mixed bromide and iodide content migrate to form iodide-rich and bromide-rich regions, which changes the absorption bands significantly. Moreover, the iodide-rich regions have a lower Helmholtz energy under illumination than bromide-rich regions, which causes the iodide-rich regions to act as an electron trap. This effect is confirmed experimentally: the photoluminescence yield of previously well-mixed perovskite material shifts to more characteristic iodide peaks after illumination.²⁸

2D perovskite solar cells

Efforts have been made to circumvent the undesired effects of ion migration. One of these approaches is the development of novel 2D perovskite layers, which are separated by organic spacer molecules as seen in Figure 3. In such structures, some of the small A-site cations of the perovskite are replaced by larger organic cations. Depending on the amount of organic spacer, the perovskite forms 2D-structures with a different value for n , with n representing the amount of octahedral perovskite sheets that are found between the organic spacer cations.³⁰ $n = 1$ thus represents one layer of octahedral perovskite separated by organic spacers, $n = 2$ two layers of octahedral perovskite and $n = \infty$ represents 3D perovskite.

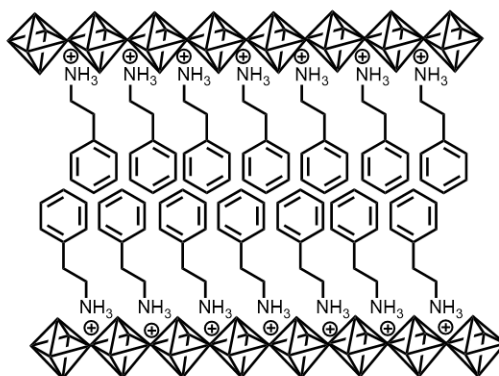


Figure 3 – Simplified depiction of 2D perovskite structure ($n=1$), here PhenEthylAmmonium (PEA) is used, note that a range of spacers can be used.

There are strong indications for reduced ion migration in full 2D perovskite systems. One study compared the conductivity of 2D ($n = 4$) and 3D perovskite systems over a temperature range. In the 3D system, ionic conductivity started dominating at temperatures above 260 K, resulting in a change of the slope in the temperature-conductivity plot. In the 2D system, there was no change in slope at all, attributed to the absence of any ionic conductivity and thus suppressed ion migration.³¹

Reduced ion migration was also observed in 2D structures by examining phase-separated films. Two separate perovskite films with pure MAPbI_3 and MAPbBr_3 were physically connected and treated thermally (23-140 °C for 60-120 minutes). To track the halide migration, absorption spectra were recorded. While mixing of the bromide and iodide halides was observed for $n=10$, $n=6$ and $n=1$, the kinetics of this halide

interchange were altered by changing the value of n . By plotting the rate against the annealing temperature, Arrhenius plots were obtained, revealing the n -dependent activation energies of ion migration (53.5 kJ/mole for $n=\infty$ (3D), 58 kJ/mole for $n=10$, 67 kJ/mole for $n=6$, 71.5 kJ/mole for $n=1$).^{32,33} This trend further confirms that ion migration is reduced, or even suppressed in 2D perovskite layers. However, the 2D perovskites have a major downside; the PCE in 2D devices is significantly lower than their corresponding 3D systems. Although relatively high PCEs have been achieved (>15%) in 2D systems through crystallisation control growth perpendicular to the substrate, most PCEs achieved so far are well below their 3D perovskite equivalents.³⁴

2D/3D perovskite solar cells

Another approach to reduce ion migration and interface penetration while retaining high PCE is based on the combination of 2D perovskites and 3D perovskite. In such 2D/3D systems, the bulk of the perovskite is a 3D layer, which is only covered with a fraction of 2D perovskite between the interface and the 3D perovskite (Figure 4).³⁵

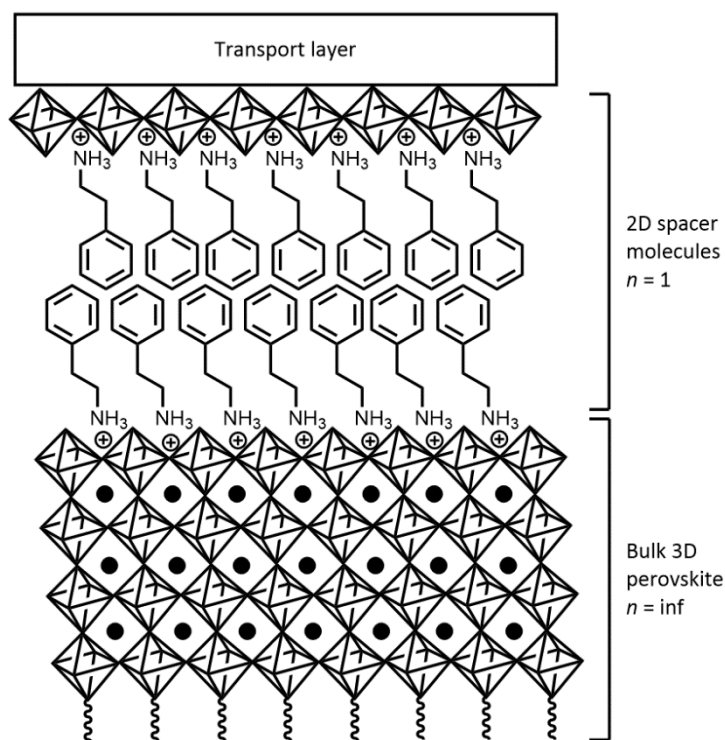


Figure 4 – Simplified depiction of a 2D/3D system, the bulk 3D perovskite system and the charge extraction layer are separated by a 2D perovskite layer, here depicted with PEA as organic spacer.

Such 2D/3D systems greatly increase the operational stability of perovskite solar cells. One example of these systems retained its PCE of >11% for >10,000h of testing under standard conditions.³⁵ Another 2D/3D system resulted in enhanced hole extraction and suppressed non-radiative recombination. This system has a PCE of over 22% and 90% PCE retention after 1000h of unsealed, humid, conditions under simulated solar radiation.³⁶ We thus focus our study on such 2D/3D perovskite systems, to benefit from their complementary benefits in high efficiency and stability.

Supramolecular design principles in 2D/3D perovskites

Similar to regular 2D systems, a range of organic spacers can be used. The efficacy of the spacers is thought to be determined by their intermolecular interaction: a stronger interaction between the molecules should facilitate a better packing, with fewer defects. To facilitate this, supramolecular design principles were applied, which will be discussed below. In this work, spacer molecules based on π - π interactions were used (Figure 5): PhenEthylAmmonium (PEA) and pentaFluorophenEthylAmmonium (FEA).³⁷ Both of these molecules have an aromatic ring for supramolecular interactions and an ethylammonium group to facilitate conformational freedom while coordinating to the perovskite octahedra. The fluorine atoms remove electron density from the aromatic ring in the FEA system.

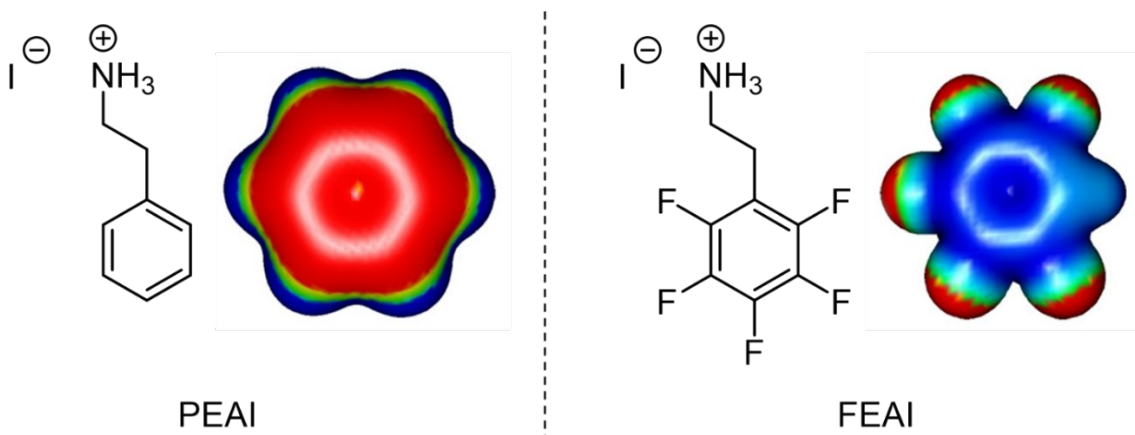


Figure 5 – The organic spacers used in this work and their respective electron density maps, red represents a high electron density, blue represents a low density. PhenEthylAmmonium Iodide (PEAI) is shown on the left and pentaFluorophenEthylAmmonium Iodide (FEAI) on the right. Electron density maps reproduced from M. Weber.³⁸

In a pure PEA-based system, there is π - π interaction between the aromatic rings (Figure 6), but the electron density is focussed on the centre of the ring, causing electron repulsion and thus decreasing the bond energy of the supramolecular bond. T-shaped stacking (Figure 6) is not possible for PEA, since the orbitals with a relatively low electron density are the in plane of the C-H bond and thus not available for electron donation from the aromatic ring from another PEA molecule.

In a pure FEA-based system, there could also be π - π interaction between the aromatic rings, but again, there is no favourable electron attraction; in these systems, it is more favourable to have T-shaped stacking (Figure 6). T-shaped stacking in this case is the interaction between one of the F-atoms, with a high electron density in outward pointing orbitals, and the ring of another FEA molecule, which has a relatively low electron density.

In the mixed scenario, the FEA and PEA can alternate to facilitate a favourable match of both the π -orbitals and the electron densities. Similar to pure PEA, the molecules are π - π stacked, but now there is electron attraction instead of repulsion due to the different electron densities in the aromatic rings. An example of this supramolecular interaction can be demonstrated by mixing the liquids hexafluorobenzene and 1,3,5-trimethylbenzene, strongly resembling FEA and PEA, respectively. The two liquids are mixed and the two molecules start alternating, facilitating a match of both the π -orbitals and the electron density. This intramolecular coordination is strong enough to result in a crystalline solid with a melting point of 34 °C.³⁹

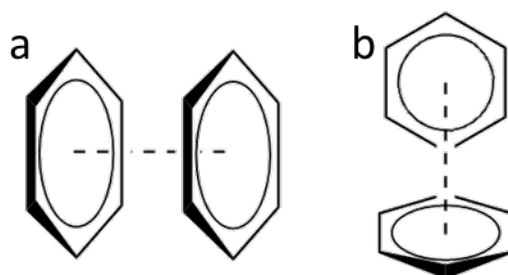


Figure 6 – Supramolecular interactions discussed in this work, a) π - π interaction, b) T-shaped stacking.

To measure the influence these design principles have on the ion migration, four types of systems (Figure 7), will be studied: 1) a reference 3D device 2) a 2D/3D system with PEA as spacer, 3) a 2D/3D system with FEA as spacer and 4) a 2D/3D system with mixed FEA/PEA (50:50 molar ratio).

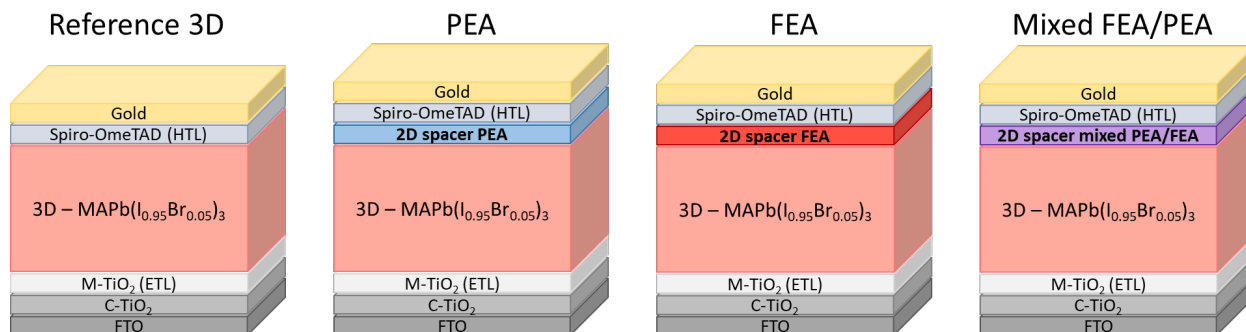


Figure 7 – In these n-i-p device architectures, the 3D perovskite is covered with an Electron Transport Layer (ETL) consisting of C-TiO₂ and M-TiO₂, and a Hole Transport Layer (HTL) consisting of Spiro-OmeTAD. The electrodes are FTO and gold. The three 2D/3D systems have a 2D perovskite layer present between the bulk 3D perovskite and the HTL.

Ion migration measurements

To gain insights in the ion migration in the 2D/3D devices, several techniques can be considered. Impedance spectroscopy, galvanostatic measurements and photothermal induced resonance microscopy all shed light on ion migration pathways.²⁵ However, it remains challenging to distinguish different processes and quantify these. This is where Transient Ion-Drift (TID) provides a powerful tool for understanding the ion migration pathways, as it can differentiate ions and processes occurring on different timescales. TID also allows the extraction of the activation energy for migration (E_A), the concentration of mobile ions (N_{ion}) and the diffusion coefficient of the ions (D).⁴⁰ The goal of this work is thus to perform TID measurement to gain insights in the ion migration mechanisms in 2D/3D systems compared to 3D systems and to determine the significance of the supramolecular design principles in the 2D layer.

Methods

Device fabrication

Devices were fabricated by Anwar Alanazi at École Polytechnique fédérale de Lausanne (EPFL), Switzerland, according to previously published procedures.^{36,41} The n-i-p device architecture is shown in Figure 7, where the HTL is Spiro-OmeTAD and the ETL is M-TiO₂ on C-TiO₂. The perovskite composition is MAPb(I_{>0.95}Br_{<0.05})₃, the perovskite film thickness is between 400 and 500 nm.

Electrical measurements

For each of these measurements, two reference 3D cells and six 2D/3D systems (2x PEA, 2x FEA, 2x mixed PEA/FEA) were measured. We performed all measurements in this work in the dark, using a commercially available DLTS setup from Semetrol. We loaded the samples into the cryostat inside of a nitrogen-based glovebox to avoid any oxygen or moisture contamination. The temperature was regulated by liquid nitrogen and an internal heating mechanism inside of the JANIS VPF-100 cryostat at pressures below 7.0×10^{-6} mbar, resulting in an available temperature range of 77–500 K.

Thermal Admittance Spectroscopy (TAS) was recorded at $V_{DC} = 0$ from 1 Hz to 500 kHz in 100 steps, using a 10 mV perturbation voltage. We repeated this measurement every 10 K, from 210 K up to 340 K.

We recorded Capacitance-Voltage (CV) measurements from -0.2 to 1.2 V (forwards) and 1.2 to -0.2 (backward) in steps of 0.01 V with a 10 mV, 10 kHz perturbation voltage. We performed these experiments at 300 K, 270 K, 240 K and 210 K.

We recorded Current-Voltage (IV) measurements from -0.2 to 1.2 V (forwards) and 1.2 to -0.2 (backward) in steps of 0.01 V, both sweeps repeated with integration times of 0.01, 0.05 and 0.1 seconds per step. We performed IV measurements at 300 K, 270 K, 240 K and 210 K.

We recorded DLTS and TID test measurement after a filling voltage pulse of 1.0 V for 1, 10, 100, 200, 500, 1000, 2000, 5000 and 10000 ms. The capacitance was measured with a 10 kHz, 10 mV perturbation voltage every 0.5 ms, 2033 data points were collected (~1s after $t=0$). The data was averaged over 20 repetitions. We performed both DLTS and TID test measurements at 300 K, 270 K, 240 K and 210 K.

We recorded TID measurements between 210 and 330 K with temperature steps of 3K. The capacitance was measured after a 2 second filling voltage pulse with a 10 kHz, 10 mV perturbation voltage every 0.5 ms. 2033 data points were collected (~1s after $t=0$), the data was averaged over 20 repetitions before moving to the next temperature. The measurements were repeated for 0.8, 1.0 and 1.2 V filling pulses. DLTS measurements were recorded similarly to TID measurement, but with a 2 ms filling voltage pulse.

TID – Data analysis

To quantify the ion migration processes, the TID transients were fitted to Equation 1, where ΔC is the amplitude of the transient at temperature T , $C(\infty)$ is the steady-state capacitance at temperature T , c_i is a fitting parameter used to calculate the diffusion coefficient in later stages, and E_a is the activation energy of ion migration.⁴²

$$f(x) = \Delta C_n * e^{-\frac{t}{c_n * T * e^{\frac{E_{an}}{k_B T}}}} + C(\infty) \quad \text{Equation 1}$$

To do so, we used scipy's differential evolution algorithm. A differential evolution algorithm is a search algorithm that iteratively improves candidate solutions based on a genetic process; "parent" solutions are combined to find the next generation of improved solutions. Such algorithms make limited assumptions about the optimisation and allow the exploration of a large parameter space in a limited timeframe.⁴³ Since this process is stochastic in nature, the fitting process is repeated at least 10 times for each datasets to acquire statistics on the obtained parameters, after which the solutions are filtered based on their cost function.⁴⁴ The cost function is a measure of how well the fitted function matches the datasets, obtained by taking the sum of the cost in all temperature traces. The cost per temperature trace is the mean square sum of the difference between data and the fitted equation. As fitting the whole dataset would lead to a cost function which is dominated by traces with higher decay amplitudes (i.e. the traces at the highest temperatures), all temperature traces were normalised to their extreme values.

The algorithm has tuneable parameters to optimise a quick route to a reliable global fit. To increase the likelihood of finding the global minimum, more iterations, a higher mutation factor and a lower tolerance factor can be set, all at the expense of computational power. After the differential evolution algorithm has found a fit, the entire procedure is repeated at least 10 times, to acquire statistics of the optimised parameters. The high-cost solutions of the global fit are then filtered, the fitted parameters of the remaining solutions are averaged and these average values are reported in this report.

A broad parameter range was applied throughout the entire fitting process to avoid bias. Typical parameter ranges are shown in Table 1.

Table 1 – Parameter ranges used for fitting procedure

ΔC_i (pF)	-30 to 2
C_i	1e-8 to 1e-4
E_{ai} (eV)	0.01 to 0.3
$C(\infty)$ offset (pF)	1e-6 to 0.5
Tolerance factor	0.002 to 0.1
Mutation factor	0.4 to 0.6
Cost Threshold	6 to 33

The maximum value of the activation energy for ion migration chosen here is lower than some of those previously reported. This range was chosen due to the observation that higher activation energies did not result in more convergence for multiple representative datasets; allowing the activation energies to

increase up to 1.2 V resulted in similar final values, far below 0.3 V, but this larger parameter space requires significantly more computational power. Moreover, changing the activation energy parameter range to 0.3 – 1.5 for E_{a1} , E_{a2} and E_{a3} one by one also did not result in a good match between the data and the fitted function.

Results and discussion

TID experiments require prior knowledge of the capacitive behaviour of the devices. Therefore, we conducted some additional experiments, which will be discussed here first, then we will elaborate on the TID theory, the TID results and finally the assignment of processes in TID to physical mechanisms in the devices.

Thermal admittance spectroscopy – TAS

TAS is a technique where the admittance of a device is measured as a function of the frequency and temperature. It allows us to determine the frequency of the perturbation voltage, with which the capacitance will be measured later. The resulting frequency dependent phase angle and capacitance of a reference 3D device are shown in Figure 8. TAS results for 2D/3D cells based on PEA, FEA and mixed PEA/FEA are shown in the Appendix, Figure 21, Figure 22 and Figure 23, respectively. We see that all devices have a high temperature dependency in the low-frequency regime and show a dip in the phase angle at intermediate frequencies.

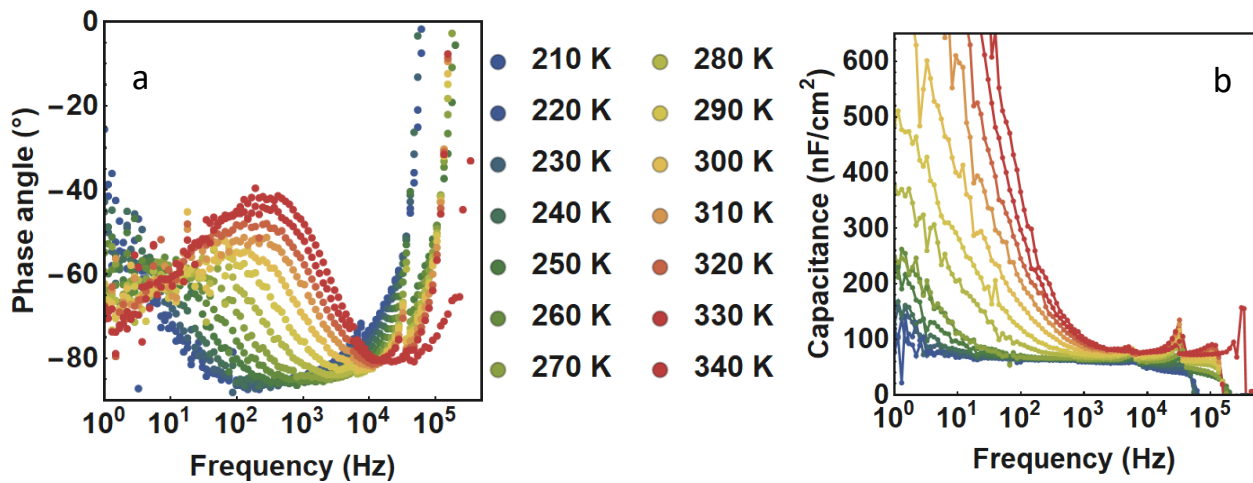


Figure 8 – Frequency dependent thermal admittance spectroscopy of a reference 3D device. a) The phase angle provides an indication of the ideality of the device as a capacitor; a perfect capacitor has a phase angle of -90° . b) The frequency dependency of the capacitance.

The phase angle describes how close the device is to an ideal capacitor; ideal capacitors have a current phase angle of -90° , caused by charge and discharge cycles as a response to the applied perturbation voltage (Figure 9).⁴⁵

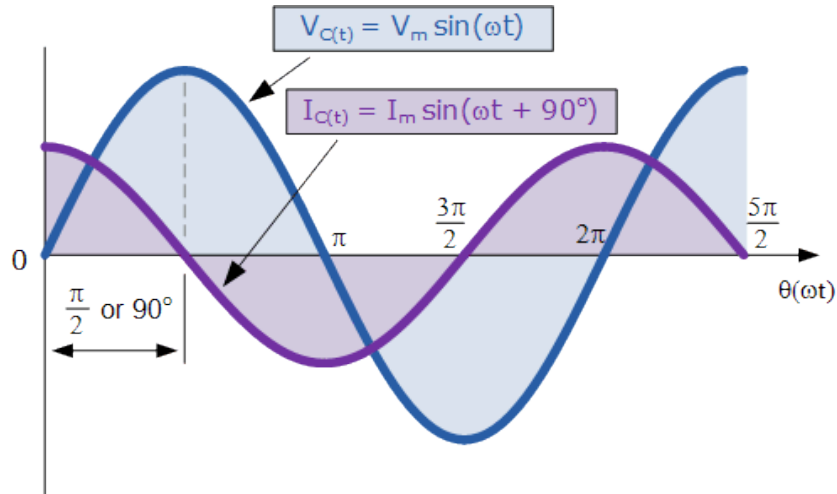


Figure 9 – Current response to voltage pulse of an ideal capacitor, resulting in a phase angle of -90° .
Reproduced from electronics-tutorials.ws.⁴⁶

We find that for most temperatures, the lowest phase angle is around 10 kHz, we thus select this frequency for the perturbation voltage to measure the capacitance in TID and DLTS measurements. From Figure 8b, it is also clear that the capacitance is relatively constant around 10 kHz. This implies that the 10 mV, 10 kHz perturbation voltage will not influence the measured capacitance in TID. This allows us to measure the capacitance change due to ionic drift instead of capacitance change due to a response to the perturbation voltage. The capacitance in the lower frequency regime ($1-10^3$ Hz) is not constant, but highly temperature dependent, caused by ion migration and dipole effects. The perturbation pulse here is sufficiently slow that ions and dipoles have time to move and thus contribute to the current response to the perturbation pulse. The higher frequency regime ($>10^5$ Hz) displays a drop in capacitance, since the series resistance dominates the signal at these frequencies.⁴⁷ The slight discontinuities are caused by our instrument switching resistors over which the capacitance is measured.

Capacitance Voltage measurements – CV

Capacitance-voltage measurements (Figure 10) are used for Mott-Schottky analysis. In such an analysis, the built-in voltage and the doping density can be extracted by solving Equation 2 within the linear regime of the CV-measurement. Here ϵ is the permittivity of the perovskite, ϵ_0 is the vacuum permittivity, q is the charge, N is the doping density, V_{bi} is the built-in voltage and V is the applied bias voltage.⁴⁸

$$C_{dl}^{-2} = \frac{2(V_{bi} - V)}{q\epsilon\epsilon_0 N} \quad \text{Equation 2}$$

However, Mott-Schottky analysis has limitations; there must be three distinct regimes in order to be performed accurately: C_g , the geometric capacitance at 0 bias, C_{dl} , the depletion capacitance and C_d , the diffusion capacitance.⁴⁸ Direct transitions from C_g to C_d are also observed for devices with a limited amount of crystal defects, resulting in a linear, apparent C_{dl} regime. Additionally, the relation between the minimal doping density and the film thickness for proper Mott-Schottky analysis has been determined by

electrostatic analysis.⁴⁹ For devices in this work with a film thickness around 450 nm, this results in a minimum doping density of 10^{15} – 10^{16} .

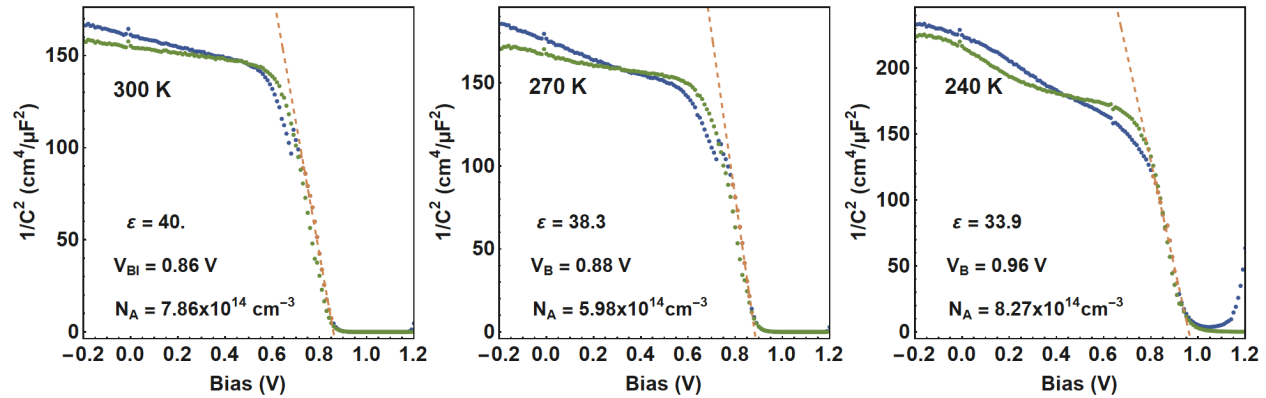


Figure 10 – Capacitance-Voltage plots of a 3D reference device (forwards sweep in green, backward sweep in blue), measured at 300, 270 and 240K, built-in voltage and doping density calculated by fitting the linear regime to Equation 2.

As seen in Figure 10, there are two main regimes in the CV-plot, the C_g at negative and low forward bias and the C_d at high bias. There is no distinct C_{dl} regime as described by Almora et al.⁴⁸ Since there is a transition from C_g to C_d , a small linear regime is seen, which has been fitted to Equation 2. The doping density in the order of 10^{14} further suggests that the doping density in these cells is too low to observe C_{dl} and is thus too low for proper Mott-Schottky analysis. The apparent depletion capacitance is likely dominated by diffusion capacitance. CV results for 2D/3D cells based on PEA, FEA and mixed PEA/FEA are shown in the appendix, Figure 24, Figure 25, and Figure 26, respectively. From these figures, it is clear that we cannot accurately extract a doping density, as the doping density that is found from the linear fit is below the theoretical minimum for devices with a film thickness of around 450 nm. The devices thus do not have a sufficient carrier density for an observable electrostatic contribution.⁴⁹

Transient Ion-Drift – TID

TID is a method to quantify the ion migration in full solar cell devices by examining the capacitance change over time after applying a bias voltage pulse. Here, a forward bias voltage is applied, this collapses the built-in field and allows all the accumulated ions to redistribute homogeneously across the perovskite layer (Figure 11). After the ions are in the new equilibrium, the voltage pulse is removed and the transient capacitance measurement starts.⁴⁵ This technique can be broken down in four stages. a) The ions are accumulated at the interface due to the internal electric field at short circuit conditions. b) A forward voltage pulse is applied, the built-in field collapses and mobile ions start to spread homogeneously. c) The mobile ions are now homogeneously distributed across the perovskite layer and the voltage pulse is stopped. d) The charge carriers distribute almost instantaneously (too fast to measure in our instrument), setting up a depletion layer and the internal electric field, causing the mobile ions to drift back to the interfaces. The capacitance measurement starts as soon as the voltage pulse is removed and we thus measure the capacitance change induced by the drift of mobile ions back to the interfaces due to the internal electric field.

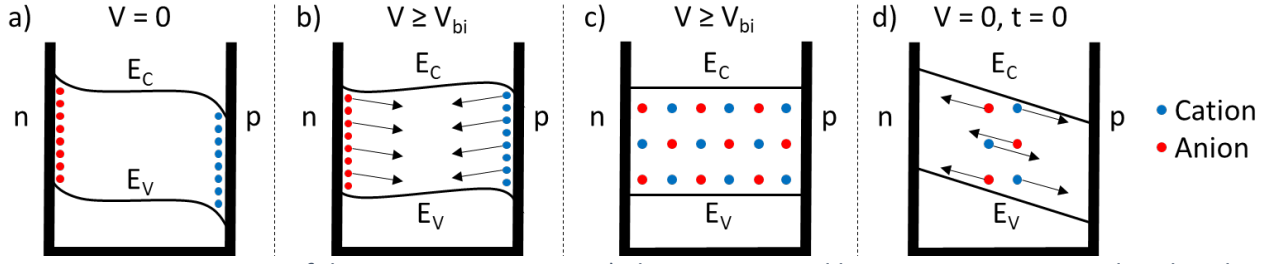


Figure 11– Four stages of the TID-measurement. a) Short circuit equilibrium, ions are accumulated at the interface. b) Forward voltage bias is applied, ions start distributing evenly throughout the perovskite layer. c) New equilibrium is established. d) Voltage bias is removed, measurement starts and ions migrate back to interfaces due to the internal electric field.⁴⁵

The almost instantaneous redistribution of the charge carriers increase the depletion width according to Equation 3, where ϵ is the permittivity of the perovskite, ϵ_0 is the vacuum permittivity, A is the active area, w_{dl} is the width of the depletion layer, q is the charge, N is the doping density, V_{bi} is the built-in voltage and V is the applied bias voltage.⁴⁰ Note that this capacitance change occurs on a timescale which is too fast for our instrument to measure.

$$C_{dl} = \frac{\epsilon\epsilon_0 A}{w_{dl}} = A \sqrt{\frac{q\epsilon\epsilon_0 N}{2(V_{bi} - V)}} \quad \text{Equation 3}$$

The mobile ions in the depletion region now drift to the interfaces of the device, changing the depletion layer width over time according to Equation 4, where N_{ion} represents the concentration of mobile ions within the depletion region and N represents the doping density. We assume here that the mobile ions pose a small perturbation to the depletion layer compared to charge carriers since the concentration of mobile ions is smaller than the doping density. Additionally, we assume that drift caused by the internal electric field dominates thermal diffusion of the ions and that the total concentration of ions remains constant.⁴⁰

$$w_{dl}(t) = \sqrt{\frac{2\epsilon\epsilon_0}{q(N \pm N_{ion}(t))}} (V_{bi} - V) \quad \text{Equation 4}$$

We then assume that the internal electric field is linear within the depletion region, is unaffected by ion migration and thus not time dependent. Therefore, we assume that the capacitance transients are only caused by effects of mobile ions according to Equation 5. For a detailed derivation of Equation 5, see Futscher et al.⁴⁰

$$C(t) = C(\infty) \pm \Delta C(1 - e^{-\frac{t}{\tau}}) \quad \text{Equation 5}$$

$C(\infty)$ is the steady-state capacitance, ΔC is the capacitance change caused by ion migration and the time constant τ is given by Equation 6, where k_B is the Boltzmann constant, T is the temperature and D is the diffusion coefficient.⁴⁰

$$\tau = \frac{k_B T \epsilon \epsilon_0}{q^2 D N} \quad \text{Equation 6}$$

The number of mobile ions can then be found by Equation 7.⁵⁰ Since we found that the doping density cannot be accurately determined by Mott-Schottky analysis in this work, the number of mobile ions will be expressed as a fraction of the doping density.

$$N_{ion}(T) = 2N \frac{\Delta C(T)}{C_{\infty}(T)} \quad \text{Equation 7}$$

The sign of the ions determines the direction of the capacitance transient; ions with the same charge as majority carriers (cations, assuming a p-type perovskite) result in an increased capacitance over time. Ions with the same charge as minority carriers (anions) result in a decreased capacitance with time.⁴⁰ This is a result of the assumption that the depletion is dominated by majority carriers. Under the assumption of a p-type perovskite, the depletion region is depleted of positively charged holes.

Figure 12 clarifies what the influence of anions is on the depletion layer width and the capacitance. After removing the voltage bias, the anions are homogeneously distributed. Once the charge carriers have redistributed to set up the built-in field, the remaining charge in the depletion layer is the sum of the remaining charge carrier density and the concentration of anions ($N + N_{anion}$). Once the anions drift out of the depletion region and accumulate at the interface, the total charge density thus reduces to only N . This leads to an increased depletion layer width and consequently a decrease of capacitance over time (see Equation 3).

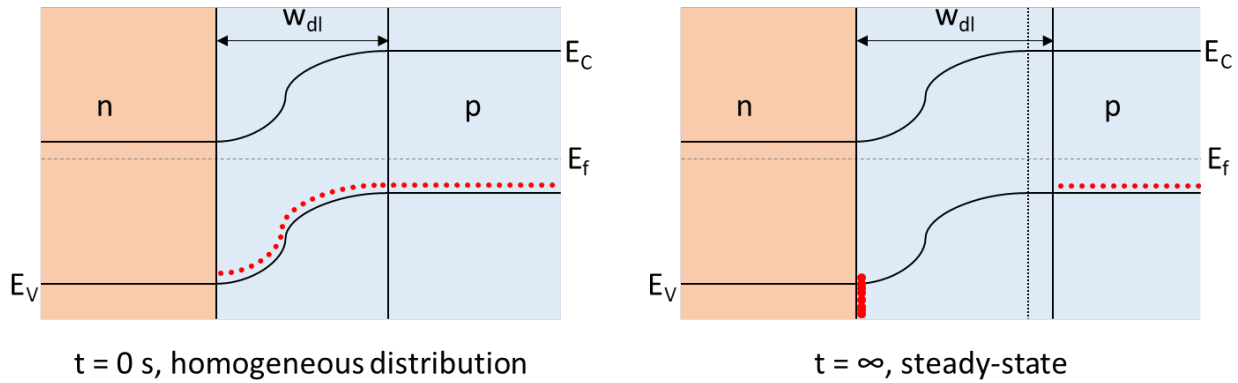


Figure 12 – Anion migration after the voltage pulse has been removed, resulting in reduced charge in the depletion region, an increased depletion width and thus a decrease in capacitance.

For cations, the remaining charge in the depletion region is given by remaining charge carrier density minus the cations ($N - N_{\text{cation}}$), since these have an opposing sign (assuming a p-type perovskite). Once the cations move out of the depletion region, the total charge in the depletion region thus increases, decreasing the depletion layer width, increasing the capacitance (Figure 13).

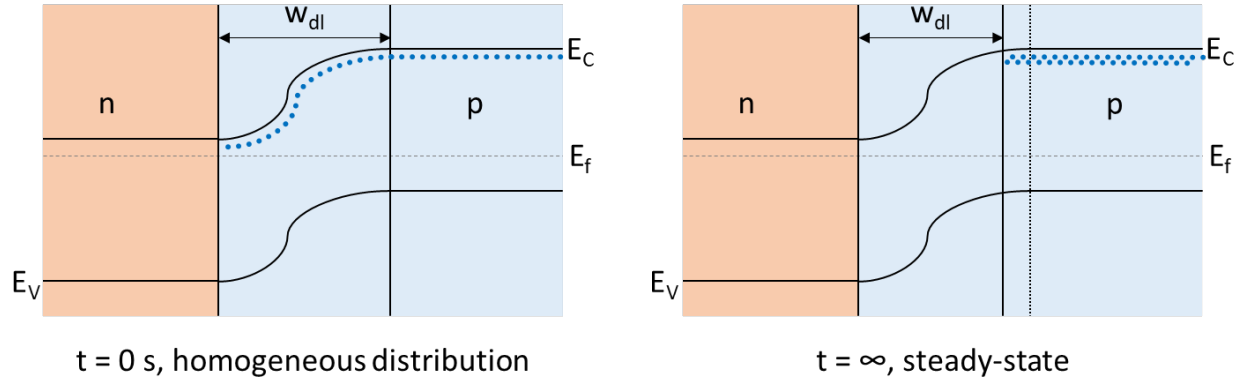


Figure 13 – Cation migration after the voltage pulse has been removed, resulting in an increased charge in the depletion region, a decreased depletion width and thus an increase in capacitance.

With these TID-principles and assumptions in mind, two devices of each kind (reference 3D, 2D/3D PEA, 2D/3D FEA and 2D/3D mixed FEA+PEA) were measured, all from different batches to observe potential batch-to-batch variations. To ensure the filling voltage was sufficient to fully collapse the depletion layer, the measurement was performed at 0.8, 1.0 and 1.2 V (Figure 14).

The 0.8 V filling pulse was not sufficient to fully collapse the built-in field, since the capacitance decay had not fully developed compared to transients that followed after a higher filling voltage.

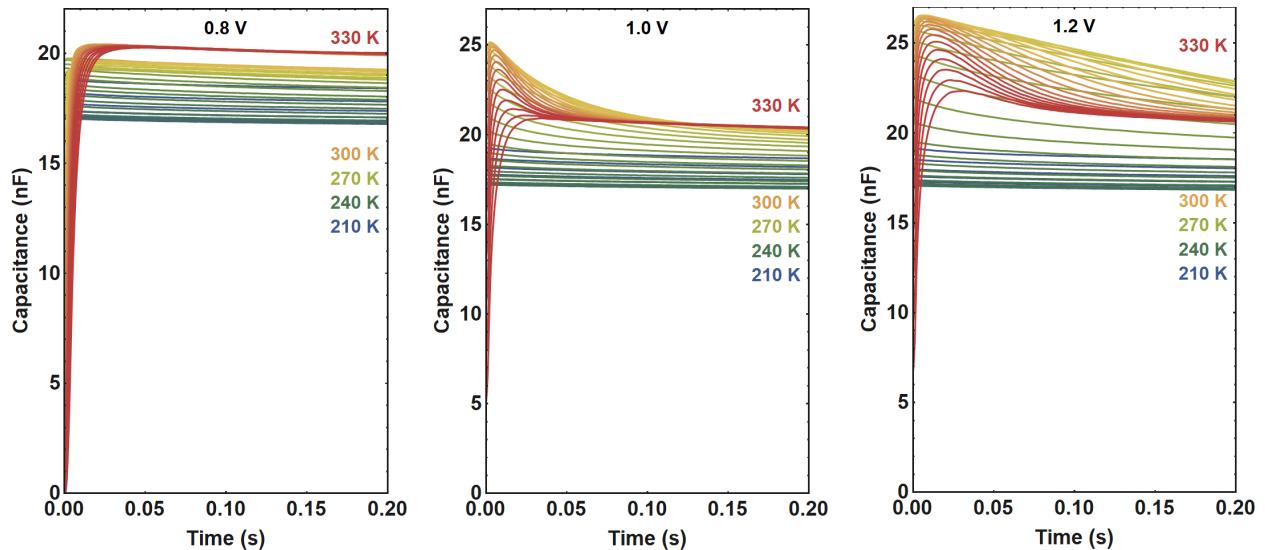


Figure 14 – Representative capacitance transients of a reference 3D device, measured after applying a 0.8, 1.0 and 1.2 V filling pulse for 2 seconds. 41 transients are plotted (210–330 K, 3 K steps) intermediate temperatures are shown to indicate the colour scheme. A rise in capacitance indicates cation migration, a decrease indicates anion migration. The capacitance change over time indicates the amount of mobile ions, the thermal evolution allows extraction of E_A . Time cut off at 0.2 s to enhance visibility.

All temperature traces display a capacitance decay over time, indicating anion migration. Two exponentials are required to properly fit this capacitance decay at higher temperatures, implying that two physical processes can be distinguished within the capacitance decay. At higher temperatures, a new positive exponent starts to develop, indicating the thermal activation of migration of a positively charged moiety. The relatively large amplitude of this positive exponent would indicate a significant amount of migration of this species.

Comparative analysis

The TID capacitance transients of the reference 3D perovskite solar cell and the 2D/3D systems are plotted in Figure 15. Although the transients are similar, visual comparison already indicates subtle differences in the transients. The amount of temperature traces with the capacitance rise event changes, as well as the slope of the rise and the decay events. The absolute value of the steady-state capacitance changes somewhat due to small differences in dielectric permittivity and film thickness.

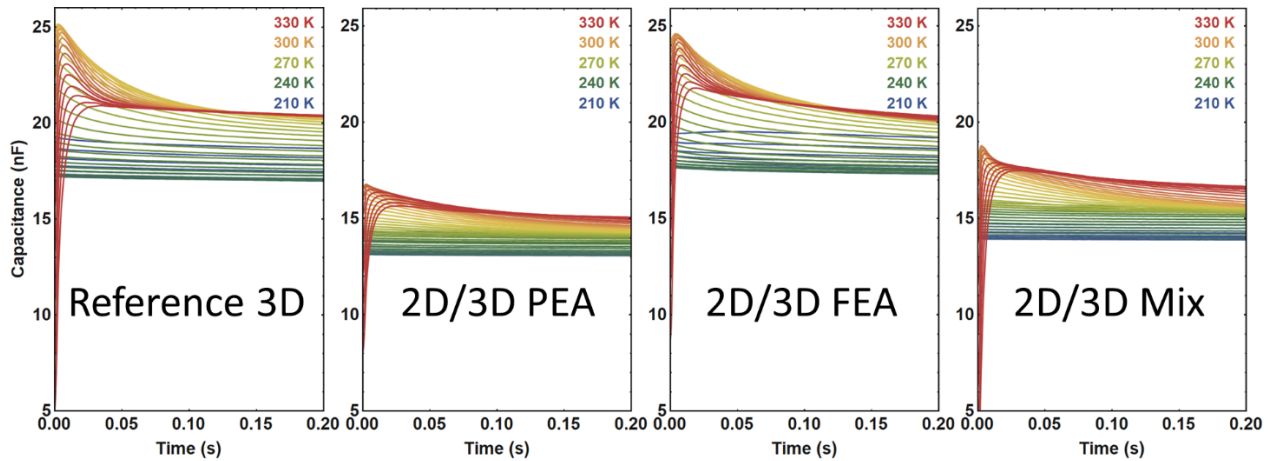


Figure 15 – TID transients for all four types of devices measured within this study, all the transients were obtained after applying a filling voltage of 1.2 V for 2 seconds. Cut off at 0.2 s for enhanced visibility.

To compare the subtle changes in the capacitance transients of all systems properly, the transients were fitted to Equation 1 in order to extract the E_A , ΔC , $C(\infty)$ and the c -coefficients (more details in the Methods section under TID – Data analysis). We found that three exponentials are required describe the data, indicating that three physical processes can be distinguished. One capacitance rise event was identified (R1) and two capacitance decay events were identified (D1 and D2).

The diffusion coefficient at 300 K was subsequently obtained from Equation 8 and Equation 9.

$$D_0 = \frac{k_B \epsilon \epsilon_0}{q^2 N c} \quad \text{Equation 8}$$

$$D = D_0 * e^{-\frac{E_A}{k_B T}} \quad \text{Equation 9}$$

Since the doping density is not known, both a lower and upper bound (10^{14} and 10^{16} cm^{-3} , respectively) were chosen to give an indication of the diffusion coefficient. The permittivity of the device was calculated from the geometric capacitance in CV-measurements. The concentration of mobile ions was then calculated as a fraction of the unknown doping density (see Equation 7).

Since the 0.8 V filling pulse was not sufficient to collapse the depletion region, only the obtained values for 1.0 V and 1.2 V were used to calculate the average activation energy and diffusion coefficient (Table 2). It is possible that only a fraction of the mobile ions was drifting in the measurements with lower filling voltage, therefore, only the values obtained for the 1.2 V filling pulse were used to calculate the average concentration of mobile ions (Table 2). Since the doping density is unknown, the concentration of mobile ions is presented as a percentage of the doping density.

Table 2 – Extracted parameters from fitting procedure of all devices, averaged over the experimentally obtained values of two cells from different batches. The calculation of the diffusion coefficient is based on the average of the lower and the upper bound of the doping density. Error bars represent the standard deviation of the mean over two devices.

	Reference 3D	2D/3D: PEA	2D/3D: FEA	2D/3D: Mixed
D D1 (cm^2/s)	$1.3 \pm 0.7 \text{ E-8}$	$1.4 \pm 0.8 \text{ E-8}$	$1.1 \pm 0.6 \text{ E-8}$	$9.0 \pm 5.0 \text{ E-9}$
D D2 (cm^2/s)	$10.0 \pm 6.0 \text{ E-8}$	$1.2 \pm 0.9 \text{ E-7}$	$7.0 \pm 4.0 \text{ E-8}$	$4.4 \pm 2.6 \text{ E-8}$
D R1 (cm^2/s)	$9.0 \pm 7.0 \text{ E-7}$	$1.1 \pm 0.9 \text{ E-6}$	$5.9 \pm 3.4 \text{ E-7}$	$1.2 \pm 0.8 \text{ E-6}$
E_A D1 (eV)	0.067 ± 0.014	0.110 ± 0.005	0.064 ± 0.013	0.1078 ± 0.0011
E_A D2 (eV)	0.134 ± 0.010	0.134 ± 0.022	0.143 ± 0.018	0.152 ± 0.018
E_A R1 (eV)	0.014 ± 0.008	0.036 ± 0.015	0.035 ± 0.032	0.041 ± 0.034
N D1 (% of N)	64 ± 5	25 ± 5	54 ± 10	28 ± 13
N D2 (% of N)	41 ± 8	19 ± 15	15 ± 1.6	29 ± 8
N R1 (% of N)	155 ± 31	119 ± 63	584 ± 456	1482 ± 160

The diffusion coefficients are relatively constant throughout the different 2D/3D systems and the reference 3D system (Figure 16), implying that the same three processes are observed in all systems. The diffusion coefficient of the process causing the capacitance rise (R1) is orders of magnitude higher than previously reported values for MA^+ , it is thus unlikely that the capacitance rise event in Figure 15 was caused by MA^+ migration.⁴⁵ The average diffusion coefficient of the first capacitance decay process (D1) of 1.18×10^{-8} resembles values previously reported for halide migration, while the second capacitance decay process (D2) has a slightly higher average diffusion coefficient of 8.35×10^{-8} .^{45,50} Since the doping density is unknown, there could be a systematic error in the diffusion coefficients reported herein. However, the constant trend reported here would remain.

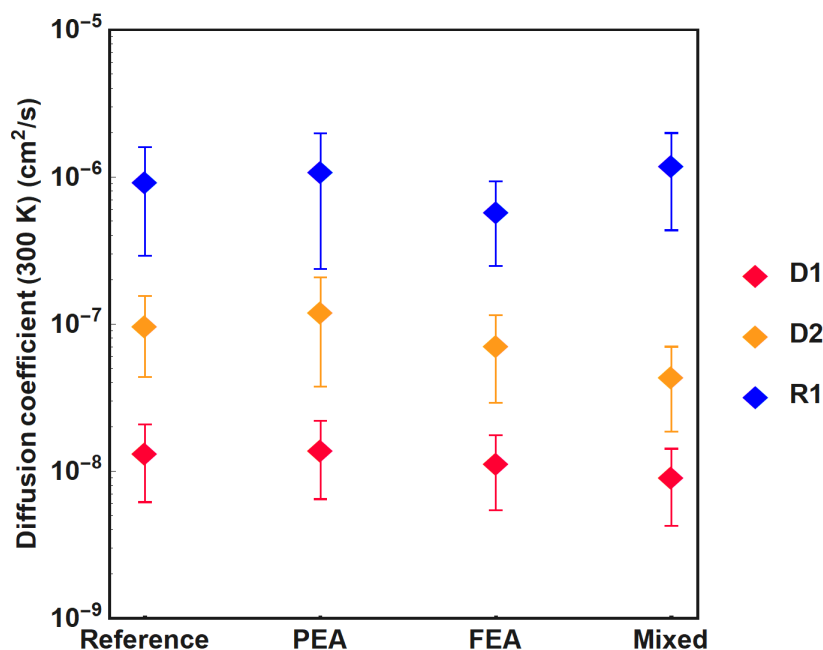


Figure 16 – Diffusion coefficients (300 K) of the mobile ions for all four systems in this work, data taken from measurements with 1.0 V and 1.2 V filling pulses on two separate cells per system (four measurements per data point). Error bars represent standard deviation of the mean.

The activation energy for R1 (Figure 17) was found to increase somewhat in the 2D/3D systems compared to the reference 3D system, but this increase has no statistical significance based on an unpaired student's t-test.⁵¹ In such a test, the probability of the data following a normal distribution is calculated; it is used to determine whether or not the means of two datasets are significantly different.⁵² Therefore, the activation energy of R1 is considered constant. However, the activation energies are roughly an order of magnitude lower than values reported for MA⁺ or Pb²⁺, further confirming that the capacitance rise events in Figure 15 are not likely an effect of migration of a cation in the perovskite.^{21,45}

For D1, an increased activation energy of migration is observed for the 2D/3D systems containing PEA ("PEA" and "Mixed"). This indicates that the π - π stacking of the 2D layer (Figure 6) could be affecting this migration process. The activation energies of D1 are in the right order of magnitude for iodide migration, although on the lower end of reported values.^{20,45} The activation energies for D2 match previously reported values for iodide migration.^{20,45} D2 shows an apparent minor increase in activation energy for the 2D/3D systems compared to the reference 3D system. However, the difference are not statistically significant.

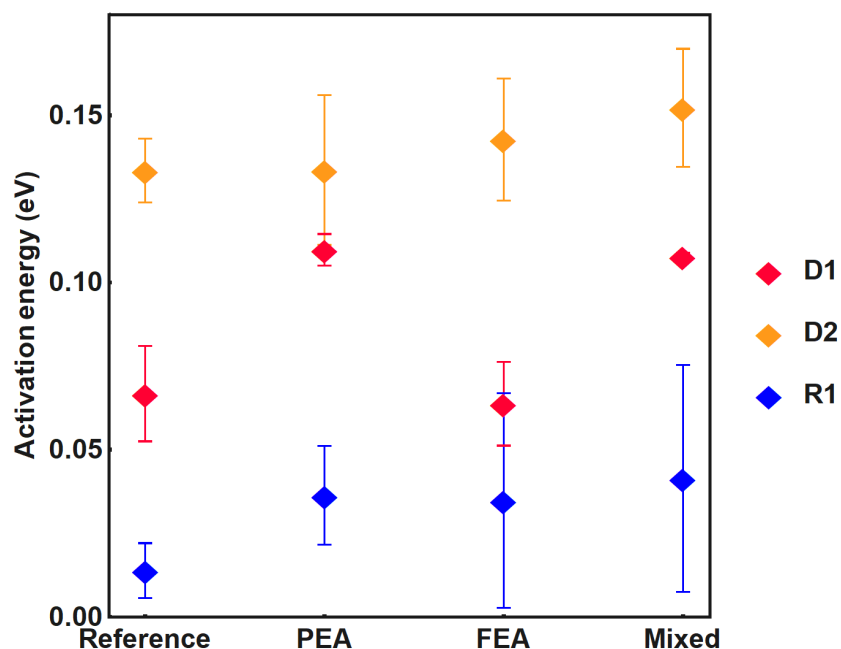


Figure 17 – Activation energies of mobile ions for all four systems in this work, data taken from measurements with 1.0 V and 1.2 V filling pulses on two separate cells per system (four measurements per data point). Error bars represent standard deviation of the mean.

In Figure 18 we present the concentration of the mobile ions as a fraction of the unknown doping density. For process R1, the concentration is higher than the doping density, which contradicts assumptions in the TID-model and again suggests a phenomenon of a different nature, which we will discuss below. Therefore, any trend in the concentration of R1 cannot be correlated to ion migration. The high apparent concentration is a direct effect of the large capacitance increase compared to the steady-state capacitance seen in Figure 15.

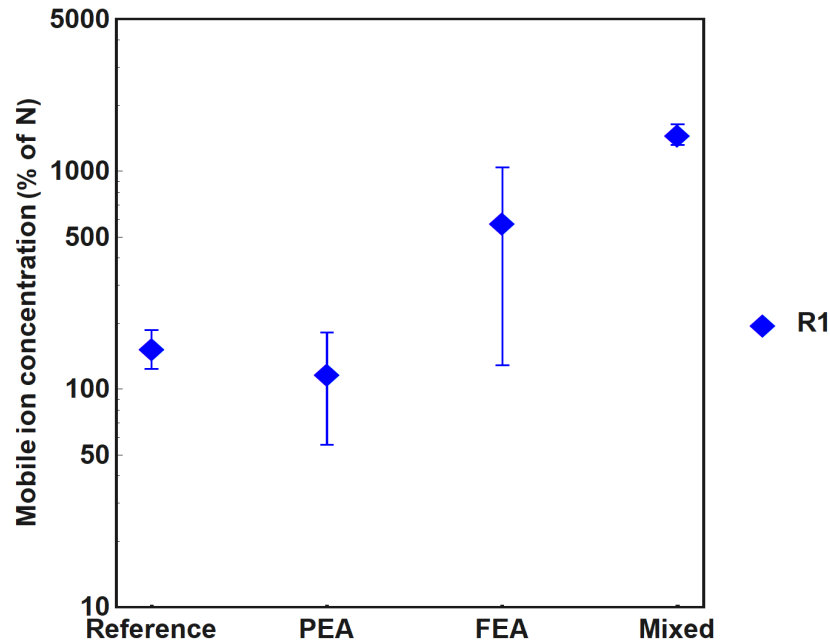


Figure 18 – Mobile ion concentrations of process R1 for all four systems in this work, data taken from measurements with a 1.2 V filling pulse on two separate cells per system (two measurements per data point), presented as a percentage of doping density, as the actual doping density is not known. Error bars represent standard deviation of the mean.

For process D1, the concentration of mobile ions (Figure 19) was found to be reduced in the 2D/3D system containing PEA and the system containing mixed PEA/FEA, compared to the reference 3D. Similar to the previously discussed activation energies, these are the systems where the molecules in the 2D-layer have a sandwich-like orientation (Figure 6) based on π - π stacking. The concentration of mobile ions in the FEA system was also found stay constant relative to the reference 3D system. The apparent decrease is not statistically significant based on a student's t-test.

For D2, the concentration of mobile ions (Figure 19) remains rather constant compared to the reference 3D systems, the apparent change is not statistically significant based on a student's t-test. We thus consider the concentration D2 to be constant throughout the measured devices.

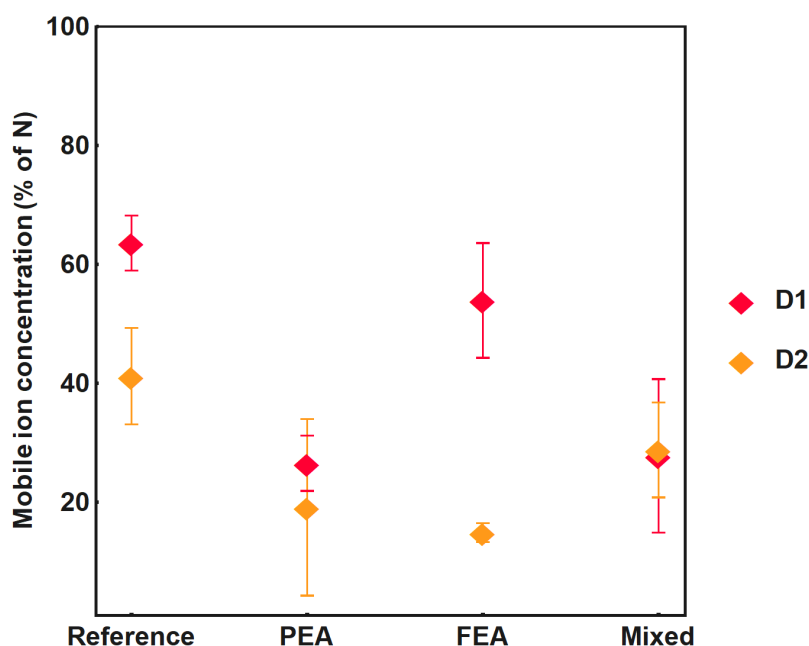


Figure 19 – Mobile ion concentrations for process D1 and D2 for all four systems in this work, data taken from measurements with a 1.2 V filling pulse on two separate cells per system (two measurements per data point), presented as a percentage of doping density, as the actual doping density is not known. Error bars represent standard deviation of the mean.

Assignment of processes to physical migration pathways

For process R1, we have seen from the low activation energy (< 50 meV) and the high diffusion coefficient ($\sim 10^{-6}$) that this process is unlikely migration of ions in the perovskite structure. The high apparent concentration also decreases the likelihood that R1 is caused by trap states or the migration of trace cations (Li^+ from Spiro-OmeTAD or H^+ from MA^+), as these processes would not result in such significant change in capacitance. We therefore cannot attribute this process to the movement of mobile ions or trap-state effects. To gain more insights in what might cause this capacitance rise event, TAS measurements were performed at $V_{\text{DC}} = 1.2$ V (see Figure 20). Since the capacitance is calculated from the impedance, it is worthwhile to investigate the impedance of the devices under the same voltage bias we apply before TID measurements.

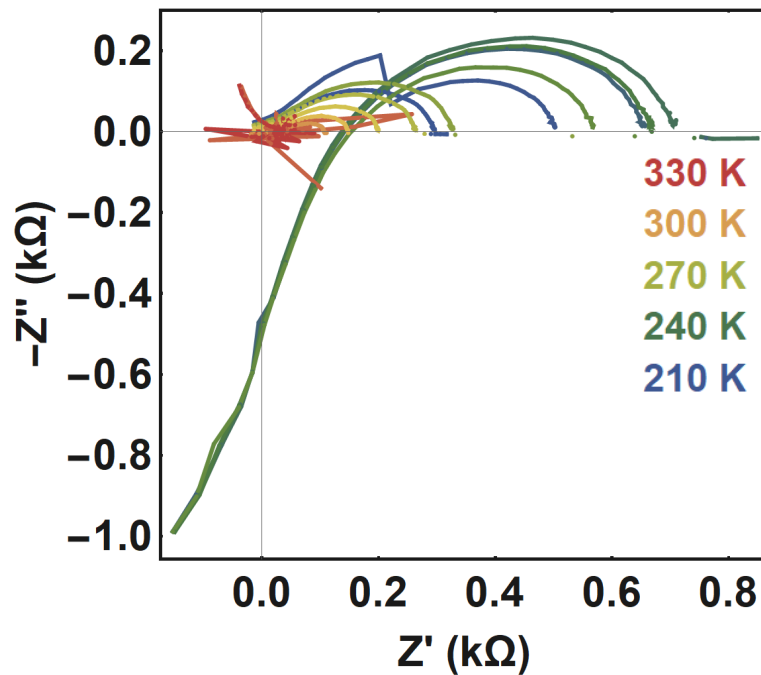


Figure 20 – Impedance spectrum of a reference 3D device, measured at $V_{\text{DC}} = 1.2$ V. Real impedance plotted on x-axis, imaginary impedance plotted on y-axis. The impedance spectrum fails to produce a trend with frequency at higher temperatures.

The impedance spectrum fails to produce a trend with frequency at temperatures above 300 K. This implies that the capacitance cannot be accurately calculated in this scenario. In the TID measurements, we start measuring the capacitance just after the voltage pulse has been removed, we thus begin the measurements in the scenario depicted in Figure 20. This strongly indicates that process R1 is another recovery mechanism from the situation under forward bias, and not the migration of ions. Which physical process is causing the impedance spectroscopy to fail at higher temperatures is currently unknown. We can speculate about known interface effects, such as charge accumulation at TiO_2 , which could result in full device depletion, or reversible redox reactions.^{53,54} While the exact mechanism causing the capacitance rise process cannot be conclusively determined, it is evident that this process is not caused by ion migration or trap states and that this process remains relatively constant in all measured devices.

The diffusion coefficient and activation energy of D1 match previously reported values of halide migration, indicating that this capacitance decay event could be caused by the migration in of iodide or bromide. Since the concentration of bromide is below 5 % and bromide is expected to migrate less than iodide, Process D1 is likely the migration of iodide.⁵⁵ This decay process was not seen in DLTS measurements (see Figure 27 and Table 3 in Appendix), further indicating that this capacitance change is unlikely caused by trapping and detrapping events. We have found that ion migration of D1 was effectively reduced in the 2D/3D systems containing PEA (“PEA” and “Mixed”). This reduction presented itself in higher activation energies for migration and a lower concentration of mobile ions in the PEA-containing 2D/3D systems. This could be due to the sandwich-like coordination of the spacer molecules (Figure 6) and/or due to other effects, such as a better stabilisation of the positive charge of the ammonium group or different crystal growth. More research is required to corroborate the exact mechanisms. However, we do observe a clear reduction in process D1 in PEA-based systems.

Lastly, the activation energy of D2 matches previously reported values of halide migration, although the diffusion coefficient is slightly higher than anticipated for halide migration. However, we cannot conclusively assign D2 to the migration of ions, as a similar decay process is also observed in the DLTS measurements of one of the reference cells (see Figure 27 and Table 3 in Appendix). Although this indicates that this process could be caused by trapping and detrapping, this process is not seen consistently in DLTS measurements within a batch or within a system throughout different batches. A more elaborate trap-state study could provide more insights on what is causing this capacitance decay event. On a general note, the activation energy, diffusion coefficient and concentration of this process remain relatively constant throughout the four systems discussed in this work, making this process unlikely to relate to the general stability gain observed in 2D/3D systems.

Conclusion and Outlook

We use Transient Ion-Drift to gain insights into the ion migration events taking place in several 2D/3D perovskite solar cells and compare these to a reference 3D device. The goal is to examine differences between the reference 3D cells and the 2D/3D systems, but also to observe to which extent the ion migration changes due to the supramolecular design of the 2D spacers. The latter is studied by using PEA, FEA and mixed PEA/FEA organic spacer molecules. By fitting the obtained capacitance transients, we have identified that the same three processes are occurring in all of the measured devices.

Process D1 was assigned to the migration of iodide, with an activation of energy between 60 and 110 meV and an average diffusion coefficient of $1.18 \times 10^{-8} \text{ cm}^2/\text{s}$. The migration of iodide is reduced in 2D/3D systems containing the PEA spacer molecule, which was expressed through higher activation energies of migration and a decreased concentration of mobile ions in the 2D/3D systems based on PEA. The exact mechanisms of this reduced ion migration are not yet known, but could be unravelled by simulations or further experimental work focussed on molecular design principles.

Process R1 is likely caused by an effect at the TiO_2 layer and had similar activation energies and diffusion coefficients throughout the systems in this work.

Process D2 cannot be conclusively assigned to the migration of ions or to trapping/detrapping events, since a process with similar activation energy and diffusion coefficient is also observed once in DLTS measurements. More elaborate trap state studies could clarify what is causing this capacitance decay

event. However, this process was found to be constant in diffusion coefficient, activation energy and concentration throughout all the measured devices, indicating that the 2D layer does not influence this process.

Together, these results show that the added 2D layer has some effect on the ion migration pathways in the studied devices, specifically the iodide migration in the PEA-containing devices. The constant trends in R1 and D2 indicate that the increased stability in 2D/3D perovskites is not due to these processes.

Besides proper assignment of R1 and D2, future work includes interface penetration studies in 2D/3D systems to study if ions can migrate through the 2D layer and react destructively with the transport layer. More knowledge about the exact mechanisms of reduced D1 migration in 2D/3D devices can also facilitate further rational design of molecular spacers.

Appendix

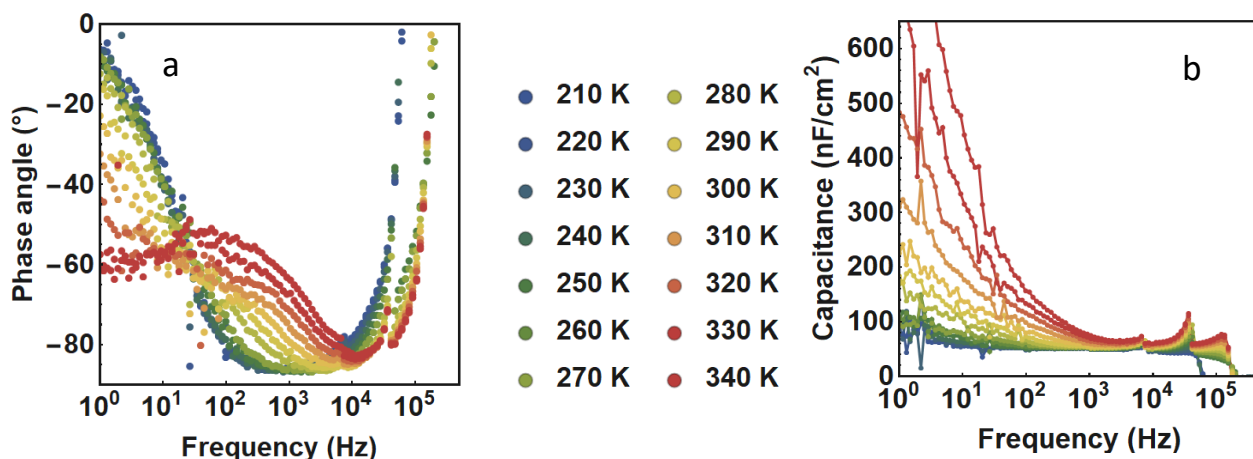


Figure 21 – Frequency dependent thermal admittance spectroscopy of a 2D/3D device based on PEA spacer molecules. a) The phase angle provides an indication of the ideality of the device as a capacitor; a perfect capacitor has a phase angle of -90° . b) The frequency dependency of the capacitance.

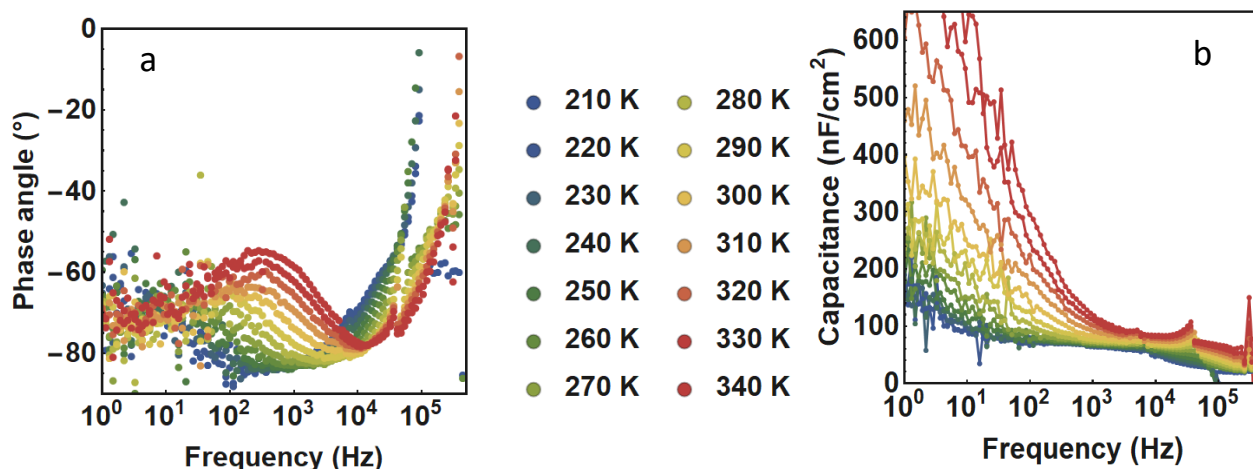


Figure 22 – Frequency dependent thermal admittance spectroscopy of a 2D/3D device based on FEA spacer molecules. a) The phase angle provides an indication of the ideality of the device as a capacitor; a perfect capacitor has a phase angle of -90° . b) The frequency dependency of the capacitance.

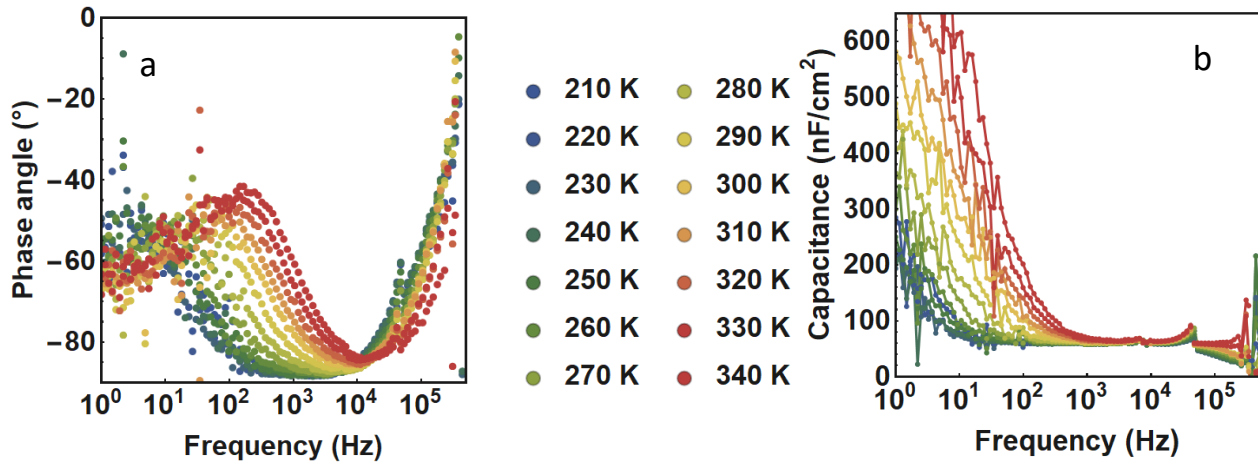


Figure 23 – Frequency dependent thermal admittance spectroscopy of a 2D/3D device based on mixed PEA+FEA spacer molecules. a) The phase angle provides an indication of the ideality of the device as a capacitor; a perfect capacitor has a phase angle of -90° . b) The frequency dependency of the capacitance.

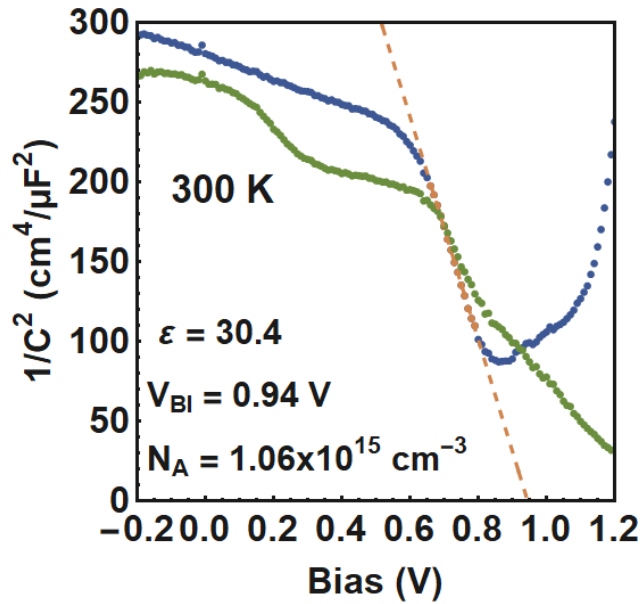


Figure 24 – Capacitance-Voltage plot of a 2D/3D device based on PEA spacers at 300 K (forwards sweep in green, backward sweep in blue), built-in voltage and doping density determined by fitting the linear regime to Equation 2. CV was also performed at, 270 K, 240 K and 210 K, but these measurements were inconclusive.

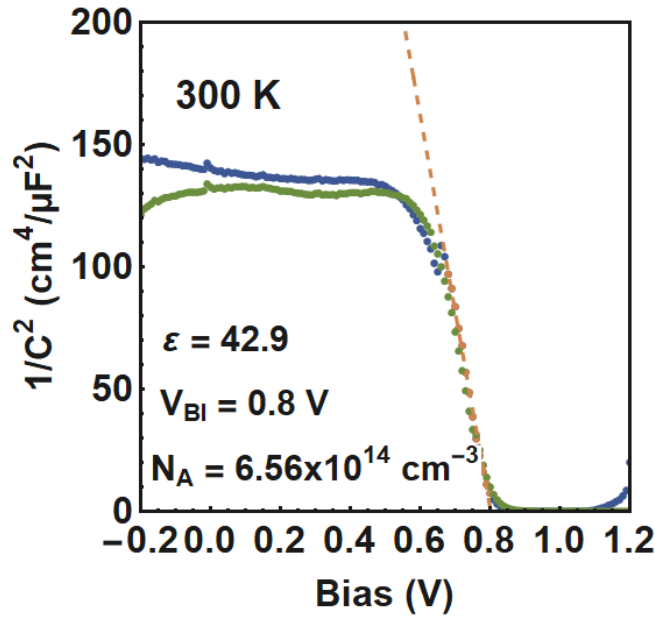


Figure 25– Capacitance-Voltage plots of a 2D/3D device based on FEA spacers at 300 K (forwards sweep in green, backward sweep in blue), built-in voltage and doping density determined by fitting the linear regime to Equation 2. CV was also performed at, 270 K, 240 K and 210 K, but these measurements were inconclusive.

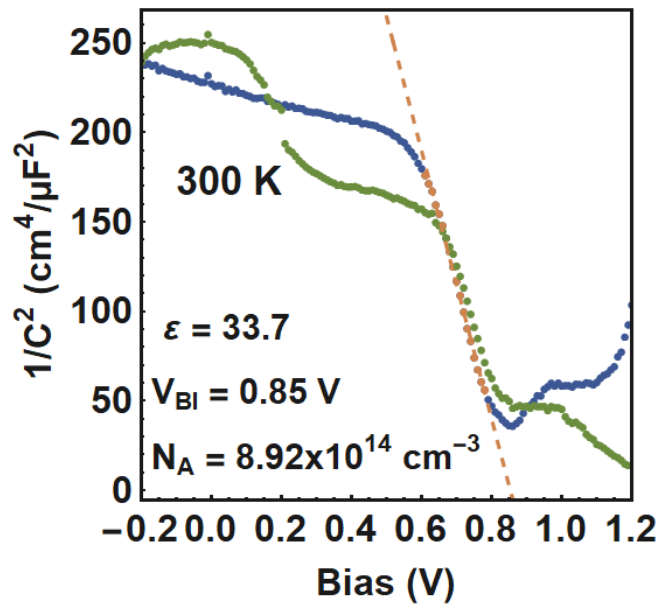


Figure 26 – Capacitance-Voltage plots of a 2D/3D device based on mixed PEA+FEA spacers at 300 K (forwards sweep in green, backward sweep in blue), built-in voltage and doping density determined by fitting the linear regime to Equation 2. CV was also performed at, 270 K, 240 K and 210 K, but these measurements were inconclusive.

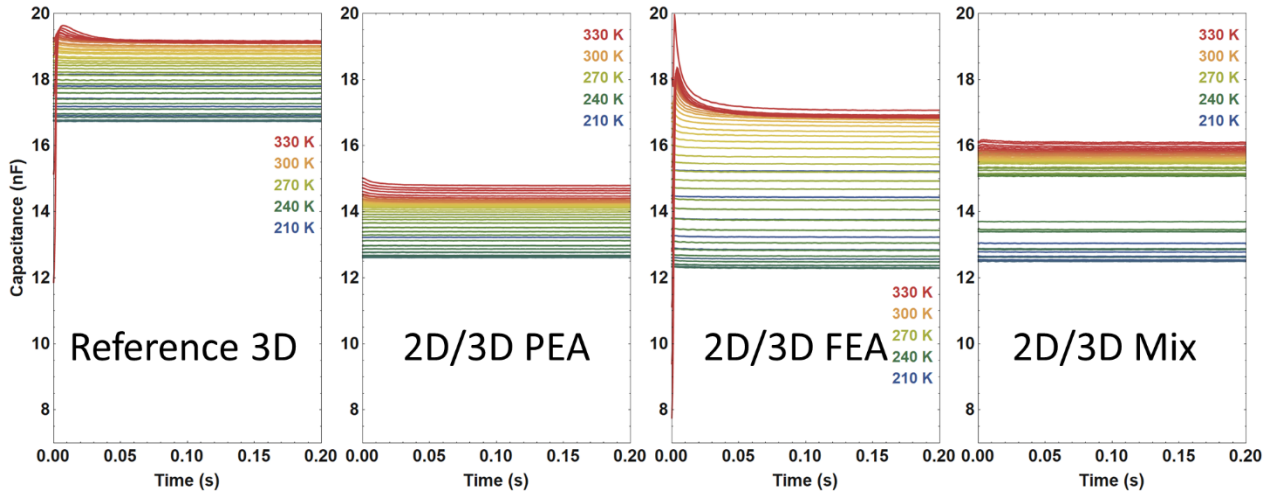


Figure 27 – DLTS transients of one batch of devices, all transients were obtained after applying a filling voltage of 1.2 V for 2 ms. Cut off at 0.2 s for enhanced visibility. Note that not every device shows capacitance rise event R1. This was not observed consistently for the same systems throughout different batches.

Table 3 – Extracted parameters from fitting procedure of DLTS data. Data shown is extracted from one batch of cells and only the DLTS measurements using a 1.2 V filling pulse.

	Reference 3D	2D/3D: PEA	2D/3D: FEA	2D/3D: Mixed
D D1 (cm²/s)	7.7 E-10	2.1 E-7	1.1 E-9	7.8 E-8
D D2 (cm²/s)	8.8 E-8	3.2 E-8	1.4 E-7	2.4 E-7
D R1 (cm²/s)	7.8 E-7	5.4 E-5	6.3 E-6	4.3 E-6
E_A D1 (eV)	0.24	0.92	0.21	0.075
E_A D2 (eV)	0.15	0.24	0.088	0.064
E_A R1 (eV)	0.065	0.0099	0.025	0.019
N D1 (% of N)	0.039	0.025	0.11	0.011
N D2 (% of N)	0.12	0.0056	0.23	0.021
N R1 (% of N)	0.48	0.44	11	5.1

References

- (1) Iacobuta, G.; Dubash, N. K.; Upadhyaya, P.; Deribe, M.; Höhne, N. National Climate Change Mitigation Legislation, Strategy and Targets: A Global Update. *Clim. Policy* **2018**, *18* (9), 1114–1132. <https://doi.org/10.1080/14693062.2018.1489772>.
- (2) Imbrie, J.; Boyle, E. A.; Clemens, S. C.; Duffy, A.; Howard, W. R.; Kukla, G.; Kutzbach, J.; Martinson, D. G.; McIntyre, A.; Mix, A. C.; Molino, B.; Morley, J. J.; Peterson, L. C.; Pisias, N. G.; Prell, W. L.; Raymo, M. E.; Shackleton, N. J.; Toggweiler, J. R. On the Structure and Origin of Major Glaciation Cycles 1. Linear Responses to Milankovitch Forcing. *Paleoceanography* **1992**, *7* (6), 701–738. <https://doi.org/10.1029/92PA02253>.
- (3) Reay, D.; Sabine, C.; Smith, P.; Hymus, G. *Intergovernmental Panel on Climate Change. Fourth Assessment Report. Geneva, Switzerland: Inter-Gov- Ernmental Panel on Climate Change. Cambridge; UK: Cambridge University Press; 2007. Available from: Wwww. Ipcc.Ch.; 2007.* <https://doi.org/10.1038/446727a>.
- (4) Kabir, E.; Kumar, P.; Kumar, S.; Adelodun, A. A.; Kim, K. H. Solar Energy: Potential and Future Prospects. *Renewable and Sustainable Energy Reviews*. Elsevier Ltd February 1, 2018, pp 894–900. <https://doi.org/10.1016/j.rser.2017.09.094>.
- (5) Ritchie, H.; Roser, M. Renewable Energy. *Our World Data* **2020**.
- (6) Lee, T. D.; Ebong, A. U. A Review of Thin Film Solar Cell Technologies and Challenges. *Renewable and Sustainable Energy Reviews*. Elsevier Ltd April 1, 2017, pp 1286–1297. <https://doi.org/10.1016/j.rser.2016.12.028>.
- (7) Polman, A.; Knight, M.; Garnett, E. C.; Ehrler, B.; Sinke, W. C. Photovoltaic Materials: Present Efficiencies and Future Challenges. *Science*. American Association for the Advancement of Science April 15, 2016. <https://doi.org/10.1126/science.aad4424>.
- (8) Roy, P.; Kumar Sinha, N.; Tiwari, S.; Khare, A. A Review on Perovskite Solar Cells: Evolution of Architecture, Fabrication Techniques, Commercialization Issues and Status. *Solar Energy*. Elsevier Ltd March 1, 2020, pp 665–688. <https://doi.org/10.1016/j.solener.2020.01.080>.
- (9) Best Research-Cell Efficiency Chart | Photovoltaic Research | NREL <https://www.nrel.gov/pv/cell-efficiency.html> (accessed Jun 17, 2021).
- (10) Perovskite (structure) ~ Detailed Information | Photos | Videos [https://alchetron.com/Perovskite-\(structure\)](https://alchetron.com/Perovskite-(structure)) (accessed Jun 1, 2021).
- (11) Wang, L.; Yuan, G. D.; Duan, R. F.; Huang, F.; Wei, T. B.; Liu, Z. Q.; Wang, J. X.; Li, J. M. Tunable Bandgap in Hybrid Perovskite CH₃NH₃Pb(Br₃-YXy) Single Crystals and Photodetector Applications. *AIP Adv.* **2016**, *6* (4), 45115. <https://doi.org/10.1063/1.4948312>.
- (12) Steirer, K. X.; Schulz, P.; Teeter, G.; Stevanovic, V.; Yang, M.; Zhu, K.; Berry, J. J. Defect Tolerance in Methylammonium Lead Triiodide Perovskite. **2016**, *1*, 28. <https://doi.org/10.1021/acsenergylett.6b00196>.
- (13) Unger, E. L.; Kegelmann, L.; Suchan, K.; Sörell, D.; Korte, L.; Albrecht, S. Roadmap and Roadblocks for the Band Gap Tunability of Metal Halide Perovskites. *J. Mater. Chem. A* **2017**, *5* (23), 11401–11409. <https://doi.org/10.1039/c7ta00404d>.
- (14) Mizusaki, J.; Arai, K.; Fueki, K. Ionic Conduction of the Perovskite-Type Halides. *Solid State Ionics* **1983**, *11* (3), 203–211. [https://doi.org/10.1016/0167-2738\(83\)90025-5](https://doi.org/10.1016/0167-2738(83)90025-5).
- (15) Alsalloum, A. Y.; Turedi, B.; Zheng, X.; Mitra, S.; Zhumeckenov, A. A.; Lee, K. J.; Maity, P.; Gereige, I.; AlSaggaf, A.; Roqan, I. S.; Mohammed, O. F.; Bakr, O. M. Low-Temperature Crystallization

- Enables 21.9% Efficient Single-Crystal MAPbI₃ Inverted Perovskite Solar Cells. *ACS Energy Lett.* **2020**, 5 (2), 657–662. <https://doi.org/10.1021/acsenerylett.9b02787>.
- (16) Colella, S.; Mosconi, E.; Fedeli, P.; Listorti, A.; Gazza, F.; Orlandi, F.; Ferro, P.; Besagni, T.; Rizzo, A.; Calestani, G.; Gigli, G.; De Angelis, F.; Mosca, R. MAPbI₃-XCl_x Mixed Halide Perovskite for Hybrid Solar Cells: The Role of Chloride as Dopant on the Transport and Structural Properties. *Chem. Mater.* **2013**, 25 (22), 4613–4618. <https://doi.org/10.1021/cm402919x>.
- (17) Wang, R.; Mujahid, M.; Duan, Y.; Wang, Z.-K.; Xue, J.; Yang, Y. A Review of Perovskites Solar Cell Stability. *Adv. Funct. Mater.* **2019**, 29, 1808843. <https://doi.org/10.1002/adfm.201808843>.
- (18) Khenkin, M. V. Consensus Statement for Stability Assessment and Reporting for Perovskite Photovoltaics Based on ISOS Procedures. *Nat. Energy* **2020**, 5 (1), 35–49. <https://doi.org/10.1038/s41560-019-0529-5>.
- (19) Ball, J. M.; Petrozza, A. Defects in Perovskite-Halides and Their Effects in Solar Cells. *Nat. Energy* **2016**, 1 (11), 1–13. <https://doi.org/10.1038/nenergy.2016.149>.
- (20) Azpiroz, J. M.; Mosconi, E.; Bisquert, J.; De Angelis, F. Defect Migration in Methylammonium Lead Iodide and Its Role in Perovskite Solar Cell Operation. *Energy Environ. Sci.* **2015**, 8 (7), 2118–2127. <https://doi.org/10.1039/c5ee01265a>.
- (21) Haruyama, J.; Sodeyama, K.; Han, L.; Tateyama, Y. First-Principles Study of Ion Diffusion in Perovskite Solar Cell Sensitizers. *J. Am. Chem. Soc.* **2015**, 137 (32), 10048–10051. <https://doi.org/10.1021/jacs.5b03615>.
- (22) Meloni, S.; Moehl, T.; Tress, W.; Franckevius, M.; Saliba, M.; Lee, Y. H.; Gao, P.; Nazeeruddin, M. K.; Zakeeruddin, S. M.; Rothlisberger, U.; Graetzel, M. Ionic Polarization-Induced Current-Voltage Hysteresis in CH₃NH₃PbX₃ Perovskite Solar Cells. *Nat. Commun.* **2016**, 7 (1), 1–9. <https://doi.org/10.1038/ncomms10334>.
- (23) Delugas, P.; Caddeo, C.; Filippetti, A.; Mattoni, A. Thermally Activated Point Defect Diffusion in Methylammonium Lead Trihalide: Anisotropic and Ultrahigh Mobility of Iodine. *J. Phys. Chem. Lett.* **2016**, 7 (13), 2356–2361. <https://doi.org/10.1021/acs.jpclett.6b00963>.
- (24) Eames, C.; Frost, J. M.; Barnes, P. R. F.; O'Regan, B. C.; Walsh, A.; Islam, M. S. Ionic Transport in Hybrid Lead Iodide Perovskite Solar Cells. *Nat. Commun.* **2015**, 6 (1), 1–8. <https://doi.org/10.1038/ncomms8497>.
- (25) Zhao, Y.; Zhou, W.; Han, Z.; Yu, D.; Zhao, Q. Effects of Ion Migration and Improvement Strategies for the Operational Stability of Perovskite Solar Cells. *Physical Chemistry Chemical Physics*. 2021, pp 94–106. <https://doi.org/10.1039/d0cp04418k>.
- (26) Yuan, Y.; Chae, J.; Shao, Y.; Wang, Q.; Xiao, Z.; Centrone, A.; Huang, J. Photovoltaic Switching Mechanism in Lateral Structure Hybrid Perovskite Solar Cells. *Adv. Energy Mater.* **2015**, 5 (15), 1500615. <https://doi.org/10.1002/aenm.201500615>.
- (27) Kim, S.; Bae, S.; Lee, S.-W.; Cho, K.; Lee, K. D.; Kim, H.; Park, S.; Kwon, G.; Ahn, S.-W.; Lee, H.-M.; Kang, Y.; Lee, H.-S.; Kim, D. Relationship between Ion Migration and Interfacial Degradation of CH₃NH₃PbI₃ Perovskite Solar Cells under Thermal Conditions OPEN. <https://doi.org/10.1038/s41598-017-00866-6>.
- (28) Hoke, E. T.; Slotcavage, D. J.; Dohner, E. R.; Bowring, A. R.; Karunadasa, H. I.; McGehee, M. D. Reversible Photo-Induced Trap Formation in Mixed-Halide Hybrid Perovskites for Photovoltaics. *Chem. Sci.* **2015**, 6 (1), 613–617. <https://doi.org/10.1039/c4sc03141e>.
- (29) Knight, A. J.; Herz, L. M. Preventing Phase Segregation in Mixed-Halide Perovskites: A Perspective. *Energy and Environmental Science*. Royal Society of Chemistry July 1, 2020, pp 2024–2046. <https://doi.org/10.1039/d0ee00788a>.

- (30) Smith, I. C.; Hoke, E. T.; Solis-Ibarra, D.; McGehee, M. D.; Karunadasa, H. I. A Layered Hybrid Perovskite Solar-Cell Absorber with Enhanced Moisture Stability**. <https://doi.org/10.1002/anie.201406466>.
- (31) Lin, Y.; Bai, Y.; Fang, Y.; Wang, Q.; Deng, Y.; Huang, J. Suppressed Ion Migration in Low-Dimensional Perovskites. **2021**, *14*, 11. <https://doi.org/10.1021/acsenergylett.7b00442>.
- (32) Cho, J.; Dubose, J. T.; Ngoc, A.; Le, T.; Kamat, P. V. Suppressed Halide Ion Migration in 2D Lead Halide Perovskites. *ACS Mater. Lett* **2020**, *2020*. <https://doi.org/10.1021/acsmaterialslett.0c00124>.
- (33) Elmelund, T.; Scheidt, R. A.; Seger, B.; Kamat, P. V. Bidirectional Halide Ion Exchange in Paired Lead Halide Perovskite Films with Thermal Activation. *ACS Energy Lett* **2019**, *4*, 2021. <https://doi.org/10.1021/acsenergylett.9b01280>.
- (34) Zhang, X.; Yang, T.; Ren, X.; Zhang, L.; Zhao, K.; Liu, S. Film Formation Control for High Performance Dion–Jacobson 2D Perovskite Solar Cells. *Adv. Energy Mater.* **2021**, *2021*, 2002733. <https://doi.org/10.1002/aenm.202002733>.
- (35) Grancini, G.; Roldán-Carmona, C.; Zimmermann, I.; Mosconi, E.; Lee, X.; Martineau, D.; Nabey, S.; Oswald, F.; De Angelis, F.; Graetzel, M.; Nazeeruddin, M. K. One-Year Stable Perovskite Solar Cells by 2D/3D Interface Engineering. *Nat. Commun.* **2017**, *8* (1), 1–8. <https://doi.org/10.1038/ncomms15684>.
- (36) Liu, Y.; Akin, S.; Pan, L.; Uchida, R.; Arora, N.; Milić, J. V.; Hinderhofer, A.; Schreiber, F.; Uhl, A. R.; Zakeeruddin, S. M.; Hagfeldt, A.; Ibrahim Dar, M.; Grätzel, M. *Ultrahydrophobic 3D/2D Fluoroarene Bilayer-Based Water-Resistant Perovskite Solar Cells with Efficiencies Exceeding 22%*; 2019; Vol. 5.
- (37) Deng, J. H.; Luo, J.; Mao, Y. L.; Lai, S.; Gong, Y. N.; Zhong, D. C.; Lu, T. B. π - π Stacking Interactions: Non-Negligible Forces for Stabilizing Porous Supramolecular Frameworks. *Sci. Adv.* **2020**, *6* (2), eaax9976. <https://doi.org/10.1126/sciadv.aax9976>.
- (38) One Ring to Rule Them All <https://jila.colorado.edu/news-events/articles/one-ring-rule-them-all> (accessed Jun 17, 2021).
- (39) Timmer, B. J. J.; Mooibroek, T. J. Intermolecular π - π Stacking Interactions Made Visible. *J. Chem. Educ.* **2021**, *98* (2), 540–545. <https://doi.org/10.1021/acs.jchemed.0c01252>.
- (40) Futscher, M. H.; Gangishetty, M. K.; Congreve, D. N.; Ehrler, B. Quantifying Mobile Ions and Electronic Defects in Perovskite-Based Devices with Temperature-Dependent Capacitance Measurements: Frequency vs Time Domain. *J. Chem. Phys* **2020**, *152*, 44202. <https://doi.org/10.1063/1.5132754>.
- (41) Milić, J. V.; Im, J. H.; Kubicki, D. J.; Ummadisingu, A.; Seo, J. Y.; Li, Y.; Ruiz-Preciado, M. A.; Dar, M. I.; Zakeeruddin, S. M.; Emsley, L.; Grätzel, M. Supramolecular Engineering for Formamidinium-Based Layered 2D Perovskite Solar Cells: Structural Complexity and Dynamics Revealed by Solid-State NMR Spectroscopy. *Adv. Energy Mater.* **2019**, *9* (20), 1900284. <https://doi.org/10.1002/aenm.201900284>.
- (42) `scipy.optimize.differential_evolution` — SciPy v1.6.3 Reference Guide https://docs.scipy.org/doc/scipy/reference/generated/scipy.optimize.differential_evolution.html (accessed Jun 13, 2021).
- (43) Georgioudakis, M.; Plevris, V. A Comparative Study of Differential Evolution Variants in Constrained Structural Optimization. *Front. Built Environ.* **2020**, *6*, 102. <https://doi.org/10.3389/fbuil.2020.00102>.
- (44) Biswas, P. P.; Suganthan, P. N.; Amaratunga, G. A. J. Minimizing Harmonic Distortion in Power

- System with Optimal Design of Hybrid Active Power Filter Using Differential Evolution. *Appl. Soft Comput. J.* **2017**, *61*, 486–496. <https://doi.org/10.1016/j.asoc.2017.08.031>.
- (45) Futscher, M. H.; Lee, J. M.; McGovern, L.; Muscarella, L. A.; Wang, T.; Haider, M. I.; Fakharuddin, A.; Schmidt-Mende, L.; Ehrler, B. Quantification of Ion Migration in CH₃NH₃PbI₃ Perovskite Solar Cells by Transient Capacitance Measurements. *Mater. Horizons* **2019**, *6* (7), 1497–1503. <https://doi.org/10.1039/c9mh00445a>.
- (46) AC Capacitance and Capacitive Reactance in AC Circuit <https://www.electronics-tutorials.ws/accircuits/ac-capacitance.html> (accessed Jun 1, 2021).
- (47) Von Hauff, E. Impedance Spectroscopy for Emerging Photovoltaics. **2019**. <https://doi.org/10.1021/acs.jpcc.9b00892>.
- (48) Almora, O.; Aranda, C.; Mas-Marzá, E.; Garcia-Belmonte, G. On Mott-Schottky Analysis Interpretation of Capacitance Measurements in Organometal Perovskite Solar Cells. *Cite as Appl. Phys. Lett* **2016**, *109*, 173903. <https://doi.org/10.1063/1.4966127>.
- (49) Ravishankar, S.; Unold, T.; Kirchartz, T. Comment on “Resolving Spatial and Energetic Distributions of Trap States in Metal Halide Perovskite Solar Cells.” *Science*. American Association for the Advancement of Science February 26, 2021. <https://doi.org/10.1126/science.abd8014>.
- (50) McGovern, L.; Koschany, I.; Grimaldi, G.; Muscarella, L. A.; Ehrler, B. Grain Size Influences Activation Energy and Migration Pathways in MAPbBr₃ Perovskite Solar Cells. *J. Phys. Chem. Lett.* **2021**, *12*, 2423–2428. <https://doi.org/10.1021/acs.jpcllett.1c00205>.
- (51) t Test calculator <https://www.graphpad.com/quickcalcs/ttest1/> (accessed Jun 17, 2021).
- (52) Kim, T. K. T Test as a Parametric Statistic. *Korean J. Anesthesiol.* **2015**, *68* (6), 540–546. <https://doi.org/10.4097/kjae.2015.68.6.540>.
- (53) Garcia-Belmonte, G.; Bisquert, J. Distinction between Capacitive and Noncapacitive Hysteretic Currents in Operation and Degradation of Perovskite Solar Cells. *ACS Energy Letters*. American Chemical Society October 14, 2016, pp 683–688. <https://doi.org/10.1021/acsenergylett.6b00293>.
- (54) Carrillo, J.; Guerrero, A.; Rahimnejad, S.; Almora, O.; Zarazua, I.; Mas-Marza, E.; Bisquert, J.; Garcia-Belmonte, G. Ionic Reactivity at Contacts and Aging of Methylammonium Lead Triiodide Perovskite Solar Cells. *Adv. Energy Mater.* **2016**, *6* (9), 1502246. <https://doi.org/10.1002/aenm.201502246>.
- (55) McGovern, L.; Futscher, M. H.; Muscarella, L. A.; Ehrler, B. Understanding the Stability of MAPbBr₃ versus MAPbI₃: Suppression of Methylammonium Migration and Reduction of Halide Migration. *J. Phys. Chem. Lett.* **2020**, *11* (17), 7127–7132. <https://doi.org/10.1021/acs.jpcllett.0c01822>.

Acknowledgements

I would like to thank **Bruno Ehrler** for providing me with the opportunity of this project, his excellent scientific and personal supervision and the many nice discussions. I am also grateful for the supervision **Lucie McGovern** has provided me during this project, she has taught me almost everything that I know and is a great friend! Of course I would also like to thank our collaborators at EPFL, **Jovana Milic** and **Anwar Alanazi**, for providing the cells and showing me how supramolecular design principles can be applied truly anywhere. I want to thank my examiners **René** and **Erik** for taking the time to assess this work and for the nice discussions. Thanks **Gianluca** for working on the differential evolution algorithm with me! You have provided the group and me with a powerful tool that will be used a lot more in the future. I also want to thank **Christian** for many nice discussions and for stepping up to become part-time supreme leader! I am also grateful to **Moritz** for taking a deeper dive into the theory with us, it really helped me gain a more fundamental understanding. Massive thanks to **Imme**, the one person in the group that I knew before starting here, your constant interest in my project and our discussions on some hard-core chemistry were always amazing! I would also like to thank my fellow Master's students **David** and **Toon** for the many laughs and discussions and for keeping me sane. I want to acknowledge **Marc** for his support on the lab, and for showing me that some practical problems have the simplest solutions. I also want to thank **Loreta**, **Jeroen**, **Maria**, **Benjamin**, **Hsiumin**, **Maria** and **Menke** for being great friends and providing an excellent atmosphere to learn in, even during a pandemic.